NTNU
Norwegian University of
Science and Technology

Design of an End-Pumped Laser Source for Generation of High-Energy Nanosecond Pulses at 1.6 μm Wavelength

Håkon Strand Klausen

Preface

This Master's thesis in physics was written during the autumn of 2015 for the Natural Science with Teacher Education program (MLREAL) at NTNU. It was done in cooperation with the laser group at Forsvarets Forskningsinstitutt (FFI). FFI provided all necessary equipment and software licenses required.

This thesis treats topics related to laser physics and nonlinear optics, and is presumed to be read by a common university level physics student. The reader is assumed to have fundamental knowledge about topics such as electromagnetism, quantum mechanics and optics. It is not assumed that the reader has extensive knowledge specifically about lasers or nonlinear optics.

Kjeller, December 8, 2015

Håkon Strand Klausen

i

Acknowledgements

Problem description

A pulsed laser source emitting nanosecond pulses at $1.6\,\mu$m wavelength has important applications within laser based distance measurements. Due to a lack of appropriate direct laser sources at this wavelength, it is necessary to reach this wavelength range by nonlinear frequency conversion. One device for achieving this is an intra-cavity optical parametric oscillator (OPO), where a nonlinear crystal, e.g. $KTiOAsO_4$, is placed inside the laser cavity for efficient frequency conversion of the laser beam.

This assignment involves:

1. Design of a Q-switched end-pumped $Nd:LiYF_4$ laser, with special emphasis on optimizing conversion efficiency and beam quality, and studying thermal lensing effects.

2. Investigation of how to efficiently convert the wavelength of the $Nd:LiYF_4$ laser using an intracavity nonlinear crystal.

3. If time permits, building a prototype of the intra-cavity OPO and characterize its performance.

Sammendrag

En numerisk modell for å simulere en pulset laser er blitt implementert. Den modellerte laseren kan generere pulser med en varighet på et noen få nanosekunder og med en justerbar bølglengde. Laseren består av en diodepumpet neodym-LiYF$_4$ laser som blir frekvenskonvertert i en intrakavitet optisk parametrisk oscillator med en KTiOAsO$_4$-krystall. Den numeriske modellen er blitt sammenlignet med eksperimentelle data for å teste gyldigheten til denne. Den har videre blitt benyttet til å optimalisere et eget design av en laser som genererer pulser med en justerbar bølgelengde rundt $1.6\,\mu$m.

Summary

A numerical model for simulating a pulsed laser has been implemented. The modelled laser can generate pulses with a duration of a few nanoseconds and a tunable wavelength. The laser consists of a diode-pumped neodymium-LiYF$_4$ laser that is frequency converted in an intracavity optical parametric oscillator with a KTiOAsO$_4$-crystal. This model was then compared to experimental results to test its validity. It was then used to optimize the design of a laser generating pulses with a tunable wavelength around $1.6\,\mu$m.

Contents

Chapter 1

Introduction

Near infrared lasers have several applications including spectroscopy, medicine and range finding. Notably, lasers in the wavelength range of 1.5-1.8 μm are well suited for range finding. This region has low absorption in the atmosphere (ref. figure 1.1), ensuring a long range. In addition, this range is considered more eye-safe than lower wavelengths [1], as it is absorbed in the cornea.

A range finder requires a high pulse energy and a good beam quality (low divergence) to ensure that it performs well over large distances. As light travels 30 cm in one nanosecond, the pulse width should only be a few nanoseconds (e.g. 10 ns) to get a good depth resolution. The pulse should have a small spectral bandwidth to get a good signal to noise ratio. In some applications, a tunable wavelength might be desired. Finally, a good overall efficiency (electrical to optical power) is desired.

Erbium doped fiber lasers [3] are one possible source for this application. Erbium-doped lasers can generate a tunable signal in the 1.5-1.6 μm spectral band. These fibers are relatively easy to produce, require no alignment of mirrors and can be made into compact devices [4]. A challenge with these fibers is the low pulse energy, particularly for short pulses [5]. This comes from the small mode area in the fiber. Higher pulse energies lead to a poor beam quality and risk of damage in the fiber.

An alternative to fibers is using a diode pumped solid state (DPSS) laser [6] in combination with an optical parametric oscillator (OPO) [7]. This combination allows for high pulse energies with a tunable wavelength.

A DPSS laser and an OPO can be combined into an intracavity optical parametric oscillator (IOPO). In an IOPO, the OPO resonator is a part of the laser resonator. An IOPO can reach higher efficiencies than an extra-cavity OPO [8]. They can also be made more compact as everything can be combined in one resonator. However, an IOPO is a complex physical system,
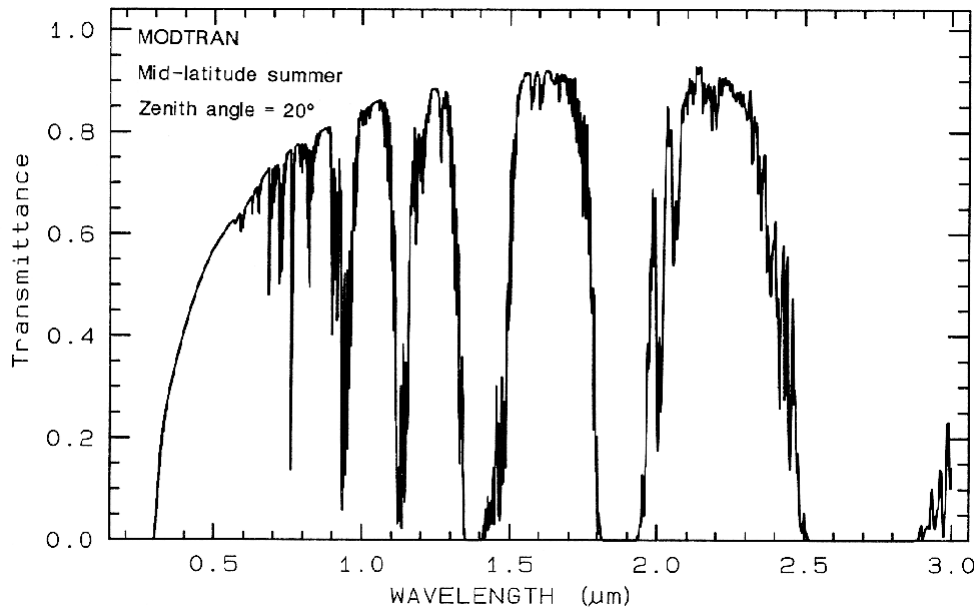
Figure 1.1: Modelled transmittance of Earth's atmosphere. Figure from [2]

linking the dynamics of the laser medium with the nonlinear interaction. It is difficult to fabricate as it requires careful alignment of components. It is also very sensitive to damage as the intensities can become very high before the conversion starts. Another major limitation is the thermal lensing in the laser rod caused by heat dissipation.

Numerical models and simulations can greatly help study IOPOs as they can solve the complex dynamics of the system. Computer modelling is also easier than laboratory tests as the former can test a wider set of parameters faster and at a lower cost. Accurate simulations can give advice when ordering expensive components and help avoid component damage.

There have been many studies regarding both DPSS lasers in general and IOPOs in particular. Thermal effects in DPSS lasers have been studied extensively, using both analytical and numerical solutions. A select examples are e.g. Cousins [9] (general theory and computer simulations on thermal lensing and thermal stresses in end pumped laser rods), Pfistner et al. [10] (comparison between theoretical model and experiments), Clarkson [11] (presents a model for thermal lensing, birefringence and energy transfer upconversion as well as measurements of the thermal lensing) and Zelenogorskii and Khazanov [12] (influence of the photoelastic effect in neodymium doped $LiYF_4$).

Likewise, there have been several studies on IOPOs. Oshman and Harris [8] first introduced intracavity OPOs and showed that their efficiency can be higher than extracavity OPOs. Falk et al. [13] further generalized the IOPO theory by implementing the interactions with a laser medium. Debuisschert et al. [14] presented some theory on a single resonant IOPO (where only one of the produced signals are coupled back in the OPO). There have been several practical demonstrations of IOPOs. Some examples are Nettleton et al. [15], Wu et al. [16], Peng et al. [17] and Bai et al. [18].

Structure of this thesis

The scope of this thesis is to present a design for a pulsed IOPO laser generating nanosecond pulses with a tunable wavelength around $1.6\,\mu$m. To reach this goal, a simulation scheme for simulating this system will be developed and tested. The scheme uses advanced software to accurately model the various effects.

The main objectives of this thesis can be summarized in the following points

- Develop a simulation model for pulsed intracavity optical parametric oscillators, incorporating laser medium interactions, thermal effects in the laser rod and nonlinear frequency conversion.

- Compare the simulation model with results from the literature.

- Use the simulation model to optimize a design of an intracavity optical parametric oscillator according to a set of given specifications.

The text starts with an introduction to elementary laser theory. In this chapter, the fundamental components of a laser will be introduced and explained. It includes a brief look at the thermal effects present in a laser rod. Expanding on this, the next chapter introduce nonlinear optics as a method for creating lasers with new wavelengths, with an introduction to the most fundamental theory on nonlinear frequency conversion. The two chapters following the theory explains the simulation method as well as the simulation goals and laser design. The simulation results are then presented along with a discussion of the strengths and weaknesses of both the model and the results.

Chapter 2

General laser theory

The acronym laser stands for light amplification by stimulated emission of radiation. Lasers differ from other sources of light due to their high degree of coherence, monochromaticity and radiance. A laser consists of several key components, the laser medium, the resonator and a pumping mechanism to supply energy. There are many different lasers (defined by their laser medium), but some of the most important are semiconductor lasers, fiber lasers and solid state lasers.

2.1 Laser amplification

Electrons bound by atoms and molecules can take on certain discrete energy levels. An electron can interact with radiation and change states depending on the nature of the interaction. The three processes that define these interactions are absorption, stimulated emission and spontaneous emission.

Assume an electron bound to an atom has two states with corresponding energies E_1 and $E_2 > E_1$. If the atom is in the state characterized by E_1, it can absorb a photon with frequency $\omega = (E_2 - E_1)/\hbar$ and be raised to the state E_2 while the photon is absorbed.

Similarly, an atom in state E_2 can interact with an incoming photon with frequency $(E_2 - E_1)/\hbar$ and emit another photon (making the total two photons) while it drops to state E_1. This is the process of stimulated emission. The atom can also spontaneously drop to the lower energy level and emit a photon. This is the process of spontaneous emission.

As stimulated emission increases the net photon number, it can be used to amplify incoming radiation. However, it can be shown that in thermodynamic equilibrium the material cannot act as an amplifier. It was shown by Einstein [19] that the rates for stimulated emission and absorption are
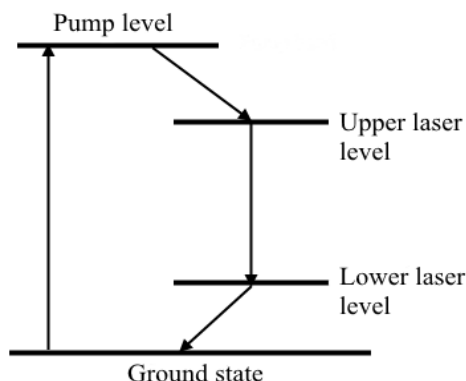
Figure 2.1: Ideal four level scheme.

equal. In other words, a photon is as likely to be absorbed by an atom in state E_1 as it is to stimulate an emission from an atom in state E_2. In thermodynamic equilibrium at temperature T, the ratio between the two populations N_i (number of elements in the state i per unit volume) is given by the Boltzmann distribution [20]

$$\frac{N_2}{N_1} = e^{-(E_2 - E_1)/k_b T},\qquad(2.1)$$

with k_b the Boltzmann's constant. This distribution implies that one cannot have a higher population in state E_2 than E_1 ($E_2 > E_1$). A lower population in the higher state will lead to incoming radiation being absorbed. A system where the upper state has a higher population is said to have a population inversion.

There are several schemes to obtain a population inversion. One example is the four level scheme. The four level scheme is presented in figure 2.1. The four levels are: the ground state, the pump level, the upper laser level and the lower laser level. Electrons are raised from the ground state to the pump level by pump photons. The pump level has a very short lifetime, and the electrons transition quickly down to the upper laser level. The upper laser level has a long lifetime, and this causes an accumulation of electrons in this level. The transition down to the lower laser level is the lasing transition. The lower level has a very short lifetime, and any electron in this state transitions quickly to the ground state.

The general concept of a laser is sketched in figure 2.2. A laser medium of length l is spaced between two mirrors M_1 and M_2 forming a resonator. The laser mode in the resonator is marked with red. The active volume (V_a)
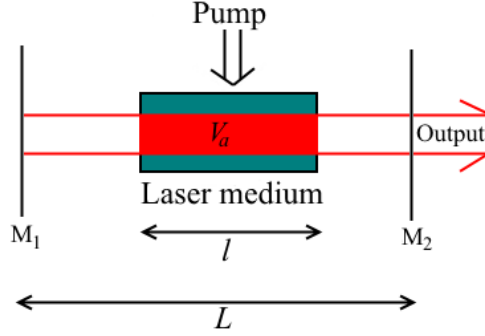
Figure 2.2: Fundamental concept of a laser. The laser medium with length l is positioned between two mirror M_1 and M_2 spaced a distance L apart. A pumping process supplies energy to the laser medium. The laser mode is marked in red.

is the volume of the mode in the laser medium. The pump supplies to the laser medium, building and maintaining the population inversion. Some of the laser is coupled out of the resonator at mirror M_2.

For an idealized four level scheme, the population in the upper laser level N and photon number ϕ are linked, and are given by the coupled rate equations [19]

$$\frac{\mathrm{d}N}{\mathrm{d}t} = R_p - B\phi N - \frac{N}{\tau}, \tag{2.2}$$

$$\frac{\mathrm{d}\phi}{\mathrm{d}t} = V_a B\phi N - \frac{\phi}{\tau_c}. \tag{2.3}$$

The various terms in this equation comes from the different mechanisms involved. The first is a pumping term, R_p. This represents a contribution to the upper laser level from the pumping, and gives the number of electrons raised to the upper laser level per second per unit volume. The second, $B\phi N$ is a term coming from stimulated emission. B is a stimulated emission rate per photon. The stimulated emission decreases the population, while increasing the photon number. V_a, is the volume of the active laser medium (ref. figure 2.2). The terms involving the lifetimes τ and τ_c represent spontaneous emissions (for (2.2)) and cavity losses (for (2.3)).

The stimulated emission rate per photon B can be expressed as [19]

$$B = \frac{\sigma l c}{V_a L_e}.$$ (2.4)

Here, σ is the stimulated emission cross section, l is the length of the laser medium, c the speed of light and $L_e = L + l(n-1)$ the optical path length of the laser cavity, with a total length L (ref. figure 2.2). The laser medium has refractive index n.

The laser starts with spontaneous emissions and build up with feedback. A wave circulating in a laser resonator will increase in amplitude from the stimulated emissions, as well as lose energy from resonator losses. The minimum population inversion required to reach a state where the gain equals the loss is called the lasing threshold.

2.2 Optical resonators

A resonator uses two or more mirrors to form wave patterns with a given transversal and longitudinal profile. It has two primary objectives. The first is to provide feedback for the laser medium. The second is to reduce the number of possible modes in the system.

The most basic resonator consists of two mirrors positioned in parallel with a distance L between them, with the most fundamental example being two plane mirrors. The first mirror is typically highly reflecting (HR), the other has a reflectance lower than unity to extract energy from the resonator. This mirror is typically called the output coupler (OC). This resonator has particularly simple longitudinal modes, with resonant frequencies $\nu = mc/2L$ (m being an integer and c the speed of light). The resonant frequencies are evenly spaced with interval $c/2L$.

A more general resonator can use two (or more) spherical mirrors. Spherical mirrors give better control over the transverse profile of the beam and are easier to align. The resonator can be either stable or unstable. In a stable resonator, the beam retraces itself after a single round trip. In an unstable resonator, an arbitrary ray will diverge away from the propagation axis.

The transverse profile of a beam in a stable resonator reproduces itself after one round trip. It can be shown that only discrete field distribution satisfies this criterion, and the distributions that does are called the transversal modes of the resonator. Higher order transversal modes have larger beam widths and higher divergence angles. The longitudinal modes of the system correspond to the resonance frequencies of the resonator.

2.3 Gaussian beams

The fundamental mode in a resonator is to a very good approximation a Gaussian beam. As the name suggests, the Gaussian beam has an amplitude $u(\vec{r})$ given by a Gaussian function in the transversal coordinates x and y [19]

$$u(\vec{r}) = \frac{w_0}{w(z)} \exp\left(-\frac{(x^2+y^2)}{w(z)^2}\right) \exp\left(-ik\frac{(x^2+y^2)}{2R(z)}\right) \exp(i\phi), \qquad (2.5)$$

with wavenumber k and the width $w(z)$, radius of the wavefronts $R(z)$, Rayleigh length z_R and phase ϕ given by

$$w(z) = w_0\sqrt{1 + \left(\frac{z}{z_R}\right)^2}, \qquad (2.6)$$

$$R(z) = z\left[1 + \left(\frac{z_R}{z}\right)^2\right], \qquad (2.7)$$

$$z_R = \frac{\pi\omega_0^2}{\lambda}, \qquad (2.8)$$

$$\phi = \arctan\left(\frac{z}{z_R}\right), \qquad (2.9)$$

λ being the wavelength of the beam. The beam width w_0 is the radius of the beam at the position $z = 0$. The beam width in (2.5) is the $1/e$-radius of the amplitude. The width of the intensity is denoted by the $1/e^2$ amplitude, a factor $\sqrt{2}$ higher. The Rayleigh length z_R is the distance in the z-direction the wave must propagate to increase its width by a factor $\sqrt{2}$. An illustration of some of the most central properties of a Gaussian beam is shown in figure 2.3.

The divergence of a Gaussian beam can be expressed using (2.6). When $z \gg z_R$ the width grows approximately linearly in z, and the resulting divergence angle θ of the beam can be approximated by

$$\theta \approx \frac{\lambda}{\pi w_0}. \qquad (2.10)$$

A Gaussian beam can also be characterized by a complex beam parameter, denoted the q-parameter of the beam. This parameter is given as

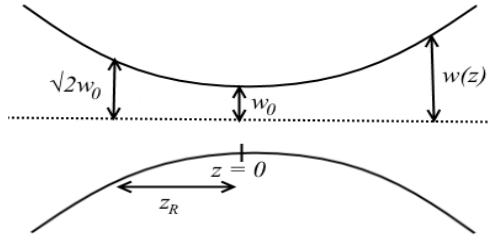$$\frac{1}{q} = \frac{1}{R} - i\frac{\lambda}{n\pi w^2}. \qquad (2.11)$$

Figure 2.3: Central properties of the Gaussian beam, showing waist w_0, Rayleigh length z_R and beam width $w(z)$.

Here, n is the refractive index of the medium. This parameter can be regarded as a complex radius of curvature of the beam. A simple law governs the change of this parameter as the beam propagates through an optical system with a specified ray transfer matrix M (see e.g. [21]). If the q-parameter of the beam is initially q_i, the new q_f is given by [19]

$$q_f = \frac{Aq_i + B}{Cq_i + D}, \qquad M = \begin{pmatrix} A & B \\ C & D \end{pmatrix}. \tag{2.12}$$

A Gaussian beam is the lowest order mode of both the Hermite-Gaussian and Laguerre-Gaussian modes. These modes are defined by the characteristic polynomial of the respective modes [22].

2.4 Resonator mode size and stability

The ABCD law (2.12) can be used to study the modes of a stable resonator. The starting point is finding the ray transfer matrix of the entire resonator, taking propagation, refraction and reflection into account. The ABCD law can then be applied to find the new q-parameter from the intial q_i. If the solution is a mode of the resonator, it must reproduce itself after a round trip. This demand means that the initial and final q-values must be equal. This results in a second order equation in q with solution

$$q = \frac{(A - D) \pm \sqrt{(D - A)^2 + 4BC}}{2C}. \tag{2.13}$$

Once the complex beam parameter is known for a single point in the resonator, it can be found for an arbitrary point by finding the required ray transfer matrix and applying the ABCD law yet again. The definition of the

9

complex beam parameter (2.11) can then be applied to find the mode size for a given complex q.

The previous discussion applies to a general, stable resonator. As seen in (2.11), the beam only has a defined width if q is a complex quantity. If q is real, the resonator is unstable and the previous discussion does not apply.

The ray transfer matrix M for a complete round trip in the resonator can also be used to check the stability of the resonator. By demanding that the ray transfer matrix does not diverge for n roundtrips as n goes to infinity, the stability criterion for a general resonator can be written as [19]

$$-1 < \left(\frac{A+D}{2}\right) < 1. \tag{2.14}$$

2.5 Beam quality

A useful tool for characterizing non-Gaussian beams is the beam quality factor M^2. This factor gives an indication of the divergence of the beam compared to a perfect Gaussian beam (given by (2.6)). The beam quality is derived from the second moment of intensity I, which is defined by [23]

$$\sigma_x^2 = \frac{\int (x-x_0)^2 I(x,y)\mathrm{d}x\mathrm{d}y}{\int I(x,y)\mathrm{d}x\mathrm{d}y}, \tag{2.15}$$

with center position x_0 and similarly for the y-direction, σ_y. Once the second moment is found, the radius of the beam can be found by the relation $W_x = 2\sigma_x$. To find the beam quality of the beam, the second moment width can be measured at several longitudinal positions. The beam quality can then be found by making a fit to a function of the form

$$W(z) = W_0\sqrt{1 + M^4\left(\frac{z}{z_R}\right)^2}. \tag{2.16}$$

When $z \gg z_R$, the square root can be approximated by $M^2 z/z_R$. Comparing this to the same relation for an ideal Gaussian beam (2.6), it can be seen that the beam diverges with a factor M^2 higher than an ideal Gaussian beam. An M^2 close to 1 means the beam behaves as a Gaussian beam to a good approximation. Higher order modes will contribute to worsen the beam quality as they increase the width and divergence of the beam. When M^2 is large, it does not say anything about the transversal profile of the beam, as there can be many transversal profiles that fit one value.
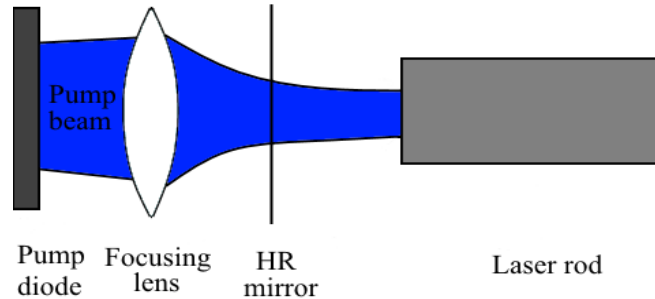
Figure 2.4: Conceptual sketch of laser end pumping. A diode laser beam enters the resonator through one of the sides and is absorbed in the rod.

2.6 Pumping schemes

The pumping process supplies energy to the system and it creates and maintains the population inversion. There are various types of pumping mechanisms, and the type of pumping is dependent on the laser medium. Diode lasers are electrically pumped, whereas solid state lasers are optically pumped. For the purpose of this text, the focus will be on optical pumping, specifically diode pumping.

There are two common methods of optical pumping. A laser (or several) can be used to pump another laser. The most usual choice for this is diode lasers. Another option is flashlamps. The main difference between these types of optical pumping is the difference in radiance (power per area per solid angle). Laser sources reach far higher radiances than flashlamps due to the confined nature of the beam as well as much smaller spectral bandwidths. Flash lamps are common due to their low cost, but their broad emission spectrum often translates to less efficient absorption and more heat deposited in the laser rod [24]. They are always used in a side-pumped geometry.

Lasers can both be used in an end pumped scheme or by side pumping. The principle of end pumping is shown in figure 2.4. Light from the pump laser (typically a diode laser) enters the resonator from one or both ends of the resonator and is absorbed in the rod. This pumping method has the advantage that the pump spot size can be tuned to the fundamental mode of the system. By choosing a laser diode with a specific wavelength, the pumping can to some extent be adapted to a single or a few strong absorption lines in the material.

2.7   Q-switching

Q-switching is used to generate high intensity laser pulses. Q-switching uses a modulator to alter between a state of high and low round trip loss in the resonator. When the loss is high, lasing is blocked and the population of the upper laser level can build up to values well above threshold. When the loss is reduced to a low value, an intense pulse develops that quickly drains the stored upper state population. The duration of the pulse is typically a few nanoseconds, and the instantaneous power can reach megawatt-levels.

There are several methods of implementing a Q-switch. Two examples are acousto-optical and electro-optical Q-switches. An acousto-optical Q-switch uses sound waves to change the the refractive index in a material. This diffracts and deflect the beam. An electro-optical Q-switch use an electric field over a crystal to modify the polarization of the beam, which can be utilized to block the wave from oscillating.

2.8   Thermal effects in laser crystals

A major limiting factor to power scaling in lasers are thermal effects in the laser medium. With increasing heat dissipation in the laser crystal, it starts to act like an aberrated lens. As the pump power scales even higher, the thermal stresses in the material can ultimately lead to crystal fracture. Thermal lensing can to some extent be compensated by introducing a lens with opposite power in the system, but the aberrations of a thermal lens are much harder to mitigate.

Most of the heat dissipated in the crystal comes from the energy difference between the pump and laser photons. This difference is called the quantum defect. The heat generated from the quantum defect can typically be 20-30% of the absorbed pump power, depending on the pump and lasing wavelength. Other processes that contribute to heat generation are energy transfer upconversion, where energy is transferred between excited ions, as well as nonradiative decays from the upper laser level.

The thermal lensing can be attributed to three mechanisms, thermo-optical effects, stress-based effects and end-face expansion. These effects vary in magnitude with the geometry and the material. The effects might also vary in sign depending on the material.

Thermo-optical effects are caused by the temperature dependence of the refractive index. The index of refraction will vary along with the temperature, and this causes shifts in the phase of the beam. The strength of the effect is given by the thermo-optic coefficient, dn/dT. The focal length of the

induced lens from the thermo-optical effect can be both positive or negative depending on the sign of the thermo-optical coefficient.

As the material heats up, it will expand. In the bulk of the material, thermal stresses caused by the expansion cause a shift in the refractive index. This is known as the photoelastic effect. The net shift in refractive index from this effect causes a contribution to the thermal lensing. In addition to thermal lensing, the photo-elastic effect also leads to thermally induced birefringence.

A third contribution to thermal lensing comes from the end face deformation. Due to the thermal expansion, the end faces will expand and deform. This can be imagined as a lens-like shape on the crystal's edges, creating a refractive interface.

There have been some measurements to determine the magnitude of the various contributions to the thermal lensing. Neodymium doped YAG (yttrium aluminium garnet) has been studied extensively due to its widespread use. Clarkson [11] estimates that approximately 86% of the thermal lensing in end-pumped Nd:YAG comes from the thermo-optical effect, with the rest from end face expansion and photoelastic effects. Koechner [24] cites a value of 74% for the thermo-optical effects, with roughly 20% coming from photo-elastic effects.

It is often hard to estimate the effects of thermal lensing in laser crystals. Thermal lenses are generally aberrated, with a radially varying focal length. This makes predicting their effect on the resonator mode difficult. Several of the parameters related to thermal lensing varies or are virtually non-existent in the literature. Some sources of heat are also difficult to estimate, such as energy-transfer upconversion.

There are some simple cases where the thermal focal length can be evaluated analytically. One such case is a uniformly pumped, very long cylindrical rod with a constant boundary temperature. It can be shown that the temperature profile has a parabolic shape [24]. This results in a uniform thermal focal length. Using a Gaussian profile on the pump beam increases aberrations significantly [11], with a radially dependent focal length.

A more realistic temperature profile in an end-pumped laser rod is shown in figure 2.5. It shows the temperature profile in a $2\,\mathrm{cm}$ long, $4\,\mathrm{mm}$ diameter 0.5% neodymium doped $\mathrm{LiYF_4}$ (YLF) rod end-pumped by a laser diode with wavelength of $808\,\mathrm{nm}$. The pump power is $30\,\mathrm{W}$, and the pump diode has a Gaussian intensity profile. The temperature profile varies both radially and longitudinally, as the pump is absorbed and drops in intensity. The juncture in the center of the rod is an artefact of the solver used.
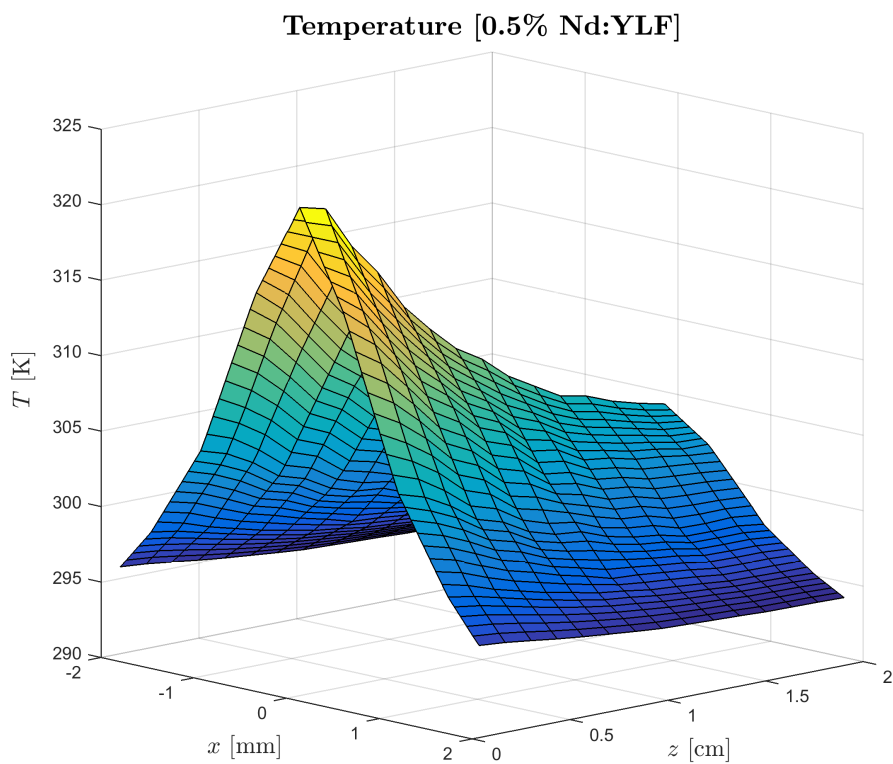
Figure 2.5: Cross section of a temperature profile in end-pumped Nd:YLF. The temperature decreases longitudinally and radially.

Chapter 3

Frequency conversion of laser radiation

3.1 Ray propagation in uniaxial and biaxial materials

The starting point for this chapter is a closer look on ray propagation in anisotropic materials. As will be shown later, this is of importance for fulfilling a criterion known as phase matching in nonlinear frequency conversion.

An isotropic material has a single value for the refractive index at a given wavelength. This index of refraction is typically given in the form of a Sellmeier equation, which is a fit to a series of measurements of the refractive index as a function of wavelength. There can exist several different Sellmeier equations for a single material.

In a uniaxial or biaxial material, the refractive index does not only vary with the frequency of the wave, but it is also dependent on the polarization of the propagating wave. This phenomenon is known as birefringence. For a uniaxial material, the refractive index differs along one of the principal axes. A wave polarized along this axis, denoted the optical axis, experiences a different refractive index compared to the other two axes. A biaxial material has a different value for each axis.

A common way of labelling the polarization of waves in a birefringent crystal is using the notation of extraordinary and ordinary waves (e-waves and o-waves). Consider propagation in one of the crystal planes in a biaxial crystal. It is common to denote the wave with polarization in the crystal plane an e-wave and the wave with the polarization orthogonal to the plane an o-wave.
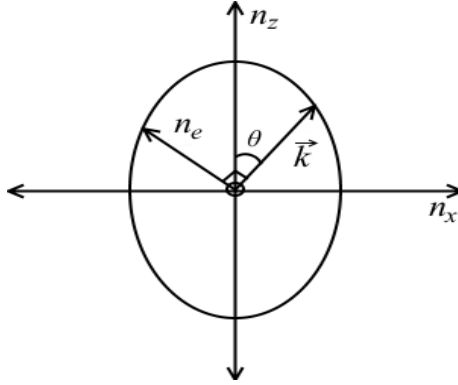
Figure 3.1: Index ellipsoid in the xz-plane. The wave with wave vector $\vec{k}$ propagates with an angle θ with respect to the z-axis.

Another way to label polarizations in birefringent materials use slow and fast axes. This labelling use the value of the refractive index experienced by the two polarizations. The polarization experiencing the lowest index of refraction is labelled fast (due to the higher phase velocity $v = c/n$) with a corresponding slow polarization.

A key concept in birefringent materials is the index ellipsoid. The index ellipsoid specifies the magnitude of the refractive index for a given propagation direction, and can be used to find the refractive index for an arbitrary ray. An illustration of the index ellipsoid is shown in figure 3.1. A wave with wave vector $\vec{k}$ propagates in the xz-plane with an angle θ with respect to the z-axis in a birefringent material. The two polarization states are either in the xz-plane (n_e) or along the y-axis (n_o).

The refractive index for the polarization in the xz-plane (e-polarization) in figure 3.1, $n_e(\theta)$, varies with the propagation angle θ and can be written as

$$\frac{1}{n_e^2(\theta)} = \frac{\sin^2\theta}{n_z^2} + \frac{\cos^2\theta}{n_x^2}. \tag{3.1}$$

Here, n_x and n_z refers to the refractive index along the x-axis and z-axis respectively. The index ellipsoid can be used to calculate the refractive index by choosing the propagation direction. This gives a gradual transition from the index along one axis to another.

For birefringent materials, the wave vector and $\vec{k}$ and the electric field for e-waves are not necessarily orthogonal [23]. As a result of this, the Poynting vector ($\vec{S} = \vec{E} \times \vec{H}$) is not parallel to the propagation direction. This leads to an effect called walk-off, where the energy of the e-wave will diverge from the
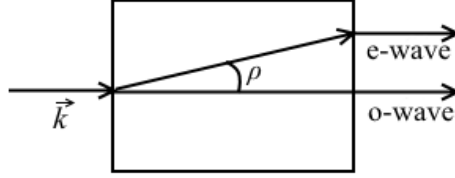
16

Figure 3.2: Walk-off. The e-wave and o-wave separate as they propagate through a birefringent crystal with a walk-off angle ρ.

propagation axis. This means that an e-wave and an o-wave will separate as they propagate in the crystal. An illustration of the walk-off effect is shown in figure 3.2.

An expression can be found for the walk-off angle ρ in a unixial crystal [23]

$$\rho = \tan^{-1}\left(\frac{n_o^2}{n_e^2}\tan\theta\right) - \theta. \tag{3.2}$$

This equation can also be used to find the walk-off angle in biaxial crystals when propagating in one of the crystal planes.

3.2 Nonlinear frequency conversion

Due to the limited number of suitable lasing transitions, many wavelengths cannot be generated directly by lasers. Instead, nonlinear frequency conversion can be used to generate these frequencies. One example of this is green laser pointers, using frequency doubled light from a diode pumped solid state laser.

In linear media, applying an electric field results in a linear response in the polarization. However, this assumption does not hold if the amplitude of the applied field becomes very large. This is often the case when illuminating the material with a laser beam. In general, the polarization $\vec{P}$ of the medium is given as a power series expansion in the electric field

$$P_i(E) = \epsilon_0\chi_{ij}^{(1)}E_j + \epsilon_0\chi_{ijk}^{(2)}E_jE_k + \epsilon_0\chi_{ijkl}^{(3)}E_jE_kE_l + \ldots \tag{3.3}$$

The Einstein notation for summation is used, meaning a sum over repeated indices. Indices refer to the three spatial directions x, y and z. The expansion coefficients $\chi^{(n)}$ are tensors of order $n+1$. They represent the n-th order susceptibility of the material. ϵ_0 is the vacuum permittivity.

17

The most common type of nonlinear frequency conversion originates from the second order term[1] in (3.3). It can be shown this applies only to non-centrosymmetric materials [23]. For a second order nonlinearity, the nonlinear polarization $\vec{P}^{\text{NL}}$ can be written as

$$P_i^{NL} = 2\epsilon_0 d_{ijk} E_j E_k. \tag{3.4}$$

The coefficient d_{ijk} is similar to the expansion coefficient $\chi_{ijk}^{(2)}s$ ($2d_{ijk} = \chi_{ijk}^{(2)}$). This coefficient is usually of the order pm/V.

The nonlinear coefficient d_{ijk} is a third order tensor, and in its most general form it has 27 components. However, symmetry considerations bring this number down to 18. The non-zero elements in tensor are determined by the point group of the material, and are tabulated for many nonlinear materials (e.g. table 3.2 in [23]). To simplify calculation, a concept known as the effective nonlinearity, d_{eff} is introduced. This is the effective nonlinear coefficient for a given interaction when propagating in a specific propagation plane.

Using the effective nonlinearity, the expression (3.4) can be rewritten to

$$P^{NL} = 2\epsilon_0 d_{\text{eff}} E^2. \tag{3.5}$$

To illustrate how a nonlinear polarization can be used to generate new frequencies, assume two plane waves with frequency ω_1 and ω_2 ($\omega_1 > \omega_2$) propagates through a medium with a nonlinear polarization given by (3.5). The electric field amplitude of the combined wave can be written as

$$E = E_1 \cos(k_1 z - \omega_1 t + \phi_1) + E_2 \cos(k_2 z - \omega_2 t + \phi_2). \tag{3.6}$$

The plane waves have wave number $k_i = \omega_i n_{/}c$ (c the speed of light and n_i the refractive index evaluated at ω_i), amplitude E_i and phase ϕ_i. The nonlinear polarization of the medium can then be found from (3.5) by squaring the expression for the field amplitude

$$\begin{aligned} P^{\text{NL}} = 2\epsilon_0 d_{\text{eff}}[&E_1^2 \cos^2(k_1 z - \omega_1 t + \phi_1) + E_2^2 \cos^2(k_2 z - \omega_2 t + \phi_2) \\ &+2E_1 E_2 \cos(k_1 z - \omega_1 t\phi_1)\cos(k_2 z - \omega_2 t + \phi_2)]. \end{aligned} \tag{3.7}$$

Setting $2\epsilon_0 d_{\text{eff}} = \gamma$, this result can be rewritten using trigonometric identities, and leads to five different contributions

---

[1]Higher order terms can also play a role, but these are not relevant in the context of this text

$$P_{\text{NL}} = \frac{\gamma}{2} E_1^2 \cos[2(k_1 z - \omega_1 t + \phi_1)] + \frac{\gamma}{2} \cos[2(k_2 z - \omega_2 t + \phi_2)]$$
$$+ \frac{\gamma}{2}(E_1^2 + E_2^2) + \gamma E_1 E_2 \cos[(k_1 + k_2)z - (\omega_1 + \omega_2)t + (\phi_1 + \phi_2)] \quad (3.8)$$
$$+ \gamma E_1 E_2 \cos[(k_1 - k_2) - (\omega_1 - \omega_2)t + (\phi_1 - \phi_2)].$$

This oscillating polarization will then radiate away energy with the corresponding frequencies [25]. The various terms in (3.8) correspond to different processes. The two first terms are second harmonic generation of $2\omega_1$ and $2\omega_2$ respectively. Second harmonic generation is a frequency-doubling process of the input frequency, and this can be seen from the expression as they oscillate with frequency $2\omega_1$ and $2\omega_2$. The third term is simply a constant term that is known as optical rectification.

The last two terms are sum frequency generation (SFG, with $\omega_1 + \omega_2$) and difference frequency generation (DFG, with $\omega_1 - \omega_2$). Note that second harmonic generation can be seen as a sub-process of sum frequency generation, where $\omega_1 = \omega_2$.

One way of implementing the nonlinear frequency conversion can be using an optical parametric oscillator (OPO). An OPO uses the premise of nonlinear frequency conversion along with an optical resonator to build a macroscopic signal from noise. An OPO can both be an external resonator (extracavity) or it can be included in the cavity of a laser to make an intracavity OPO (IOPO). In an OPO, a pump wave (ω_3) generates two new waves from noise. These waves are denoted signal (ω_2) and idler (ω_1). This process fulfils $\omega_3 = \omega_2 + \omega_1$, which can be regarded as an energy conservation statement where a pump photon splits into a signal and an idler photon.

To further investigate the nonlinear interaction, the starting point is Maxwell's equations in a dielectric medium (see f.i. [25]). These can be used to derive a wave equation in dielectric media

$$\nabla^2 \vec{E} = \frac{1}{c^2} \frac{\partial^2 \vec{E}}{\partial t^2} + \mu_0 \frac{\partial^2 \vec{P}}{\partial t^2}. \quad (3.9)$$

E is the electric field amplitude and P is the polarization (from equation (3.3). In the expression above, c is the speed of light and μ_0 is the vacuum permeability.

Assume three interacting waves with frequencies $\omega_3 > \omega_2 \geq \omega_1$ propagate through a material with a polarization given by (3.5). The electric field amplitude for wave m can be written as

$$\vec{E}_m = \hat{e}_m E_m(z, t) \exp(i k_m z), \quad (3.10)$$

with $k_m = \omega_m n(\omega_m)/c$ with $n(\omega_n) = n_m$ the refractive index and $\hat{e}_m$ a unit vector in the direction of the field. By making the slowly varying envelope approximation [23], a set of coupled amplitude equations for the three fields can be derived [26]

$$\frac{\partial E_1}{\partial z} = i\frac{\omega_1}{n_1 c} d_{\text{eff}} E_3 E_2^* \exp(i\Delta k z), \tag{3.11}$$

$$\frac{\partial E_2}{\partial z} = i\frac{\omega_2}{n_2 c} d_{\text{eff}} E_3 E_1^* \exp(i\Delta k z), \tag{3.12}$$

$$\frac{\partial E_3}{\partial z} = i\frac{\omega_3}{n_3 c} d_{\text{eff}} E_1 E_2 \exp(-i\Delta k z). \tag{3.13}$$

In the previous equations, Δk is the phase mismatch, $\Delta k = k_3 - k_2 - k_1$ and d_{eff} the effective nonlinearity. While the coupled amplitude equations can be solved exactly, there are some simplifications that can be illustrative. One such example is for difference frequency generation (with $\omega_1 = \omega_3 - \omega_2$). Making the assumption that there is no depletion of fields E_2 and E_3, the amplitude E_1 can be found by integrating (3.11)

$$E_1(z) = \frac{i\omega_1 d_{\text{eff}}}{n_1 c} E_3 E_2^* e^{i\frac{\Delta k z}{2}} \frac{\sin\left(\frac{\Delta k z}{2}\right)}{\Delta k}. \tag{3.14}$$

The corresponding intensity I_1, proportional to the square of the amplitude, can be found to be

$$I_1 = \frac{\epsilon_0 \omega_1^2 d_{\text{eff}}^2 z^2}{n_1 c} |E_3|^2 |E_2|^2 \text{sinc}^2\left(\frac{\Delta k z}{2}\right). \tag{3.15}$$

The resulting intensity is proportional to the amplitudes of the two other waves. In addition, the phase mismatch, Δk, plays a central role in the conversion. The sinc²-function has a global maximum when $\Delta k = 0$ (as $z > 0$), indicating that the optimal conversion happens when the phase mismatch is zero. This is known as the phase matching criterion.

For the case of DFG, the phase matching criterion can be rewritten as

$$\omega_3 n(\omega_3) = \omega_1 n(\omega_1) + \omega_2 n(\omega_2), \qquad \omega_3 = \omega_2 + \omega_1. \tag{3.16}$$

As the refractive index generally varies with frequency, this relation cannot be fulfilled in isotropic materials. However, this problem can be circumvented in uniaxial or biaxial materials where the refractive index can be tuned with the polarization and the propagation direction.

3.3 Phase matching

The phase matching criterion can be solved by finding the polarizations and propagation direction that satisfies the phase matching criterion (A.4). With normal dispersion, the refractive index increases with growing frequency. This results in the wave with the highest frequency having the lowest phase velocity. To counteract this, the polarization of this wave is laid along the fast axis. The remaining waves can be polarized along either the slow or fast axis. The polarization of these beams define the phase matching type. The various phase matching types are listed in table 3.1. Several properties, such as the effective nonlinearity and phase matching bandwidth are dependent on the phase matching type.

Table 3.1: Phase matching types

Type	ω_3 Pump	ω_2 Signal	ω_1 Idler
I	Fast	Slow	Slow
IIa	Fast	Slow	Fast
IIb	Fast	Fast	Slow

In a birefringent material, the propagation direction is given by the polar angle ϕ and the azimuthal angle θ. For simplicity, the propagation is chosen to lie in one of the main symmetry planes. This specifies either ϕ or θ. The angle where the phase matching criterion is fulfilled is called the phase matching angle.

It is possible to derive expressions for the phase matching angle for some types of phase matching in certain crystal planes. A derivation of the phase matching angle θ for type IIb phase matching in the xz-plane of a biaxial material is shown in the appendix (A.4). The resulting expression can be used to find the phase matching angle for DFG using a fixed pump ω_3 and a varying signal ω_2. The idler frequency is determined by $\omega_1 = \omega_3 - \omega_2$. Similar expressions exist for different phase matching types and crystal planes [27].

In figure 3.3, the phase matching angle (A.4) is shown for a specific material with varying signal wavelength. The material is KTA (potassium titanyl arsenate, $KTiOAsO_4$) with propagation in the xz-plane. The pump wavelength is fixed at 1053 nm. This corresponds to a case of a neodymium doped $LiYF_4$ pump laser undergoing difference frequency generation. The value of the phase matching angle can vary slightly if a different Sellmeier equation for the material is used.

The effective nonlinearity can be found once the phase matching type and angle are determined. For the example above, the effective nonlinearity
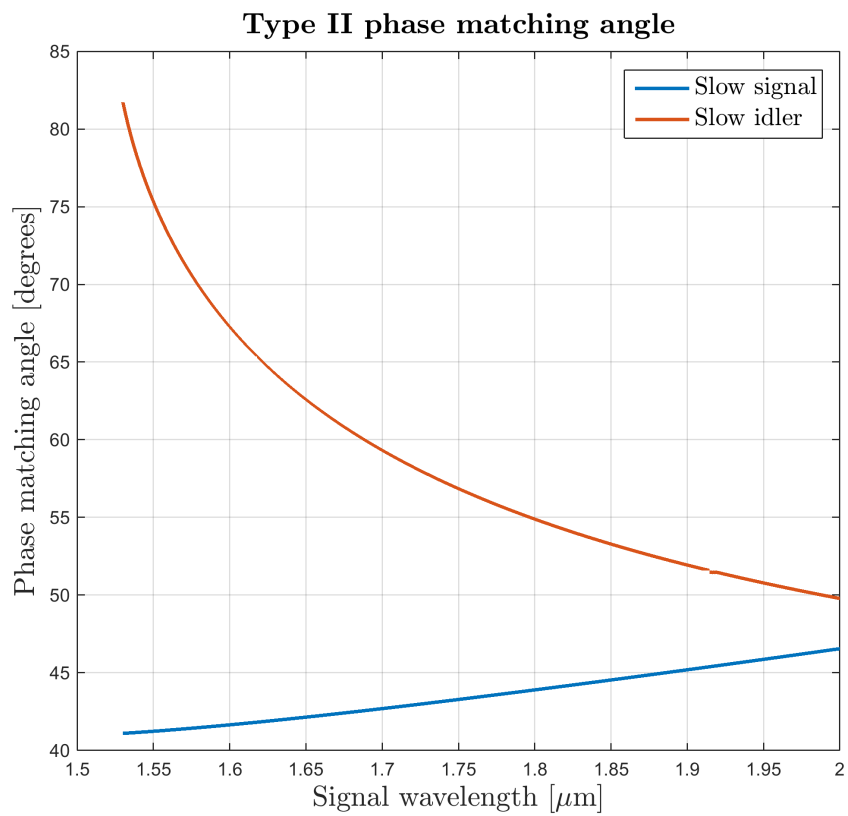
Figure 3.3: Phase matching angles as a function of signal wavelength for type IIa and IIb phase matching in KTA for propagation in the xz-plane. The pump wavelength is fixed at 1053 nm
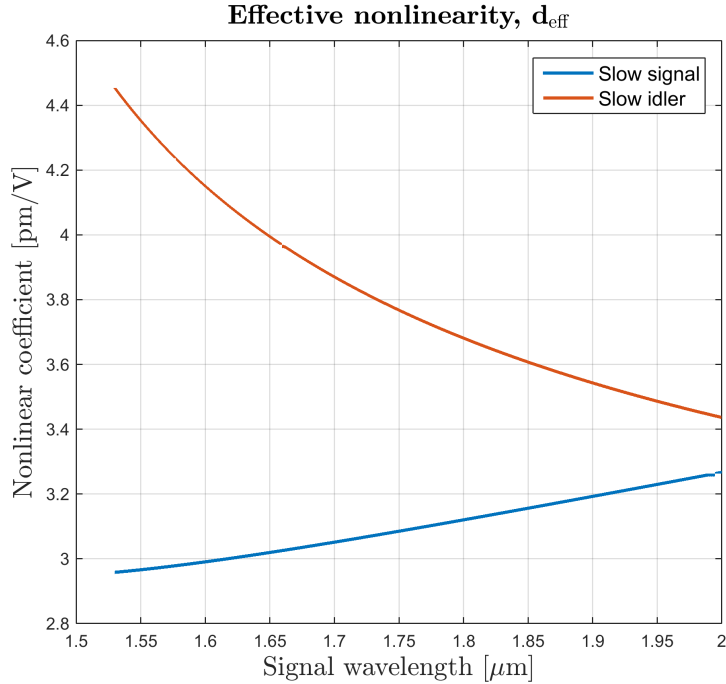
Figure 3.4: Effective nonlinearity d_{eff} for type II phase matching in KTA for varying signal wavelength. Propagation in the xz-plane. The pump wavelength is fixed to 1053 nm.

can be written as $d_{\text{eff}} = d_{24} \sin\theta$, with $d_{24} = 4.5\,\text{pm/V}$ [28]. The effective nonlinearity for type II phase matching in the xz-plane for KTA is shown in figure 3.4.

For a given nonlinear process (e.g. an OPO amplifying a signal ω_2), there is a certain phase matching bandwidth where conversion will take place. This bandwidth can be derived from (3.15), and this is done in the appendix (A.9) for a pump beam with no bandwidth. The phase matching bandwidth for type IIb phase matched KTA in the xz-plane for varying signal wavelength is shown in figure 3.5. The pump wavelength is fixed at 1053 nm.

The walk-off effect also affects the conversion. Walk-off sets a limit to the interaction length due to the physical separation of the beams. When the beams no longer overlap, the conversion will cease. This is dependent on the walk off angle (3.2) and the beam diameters.
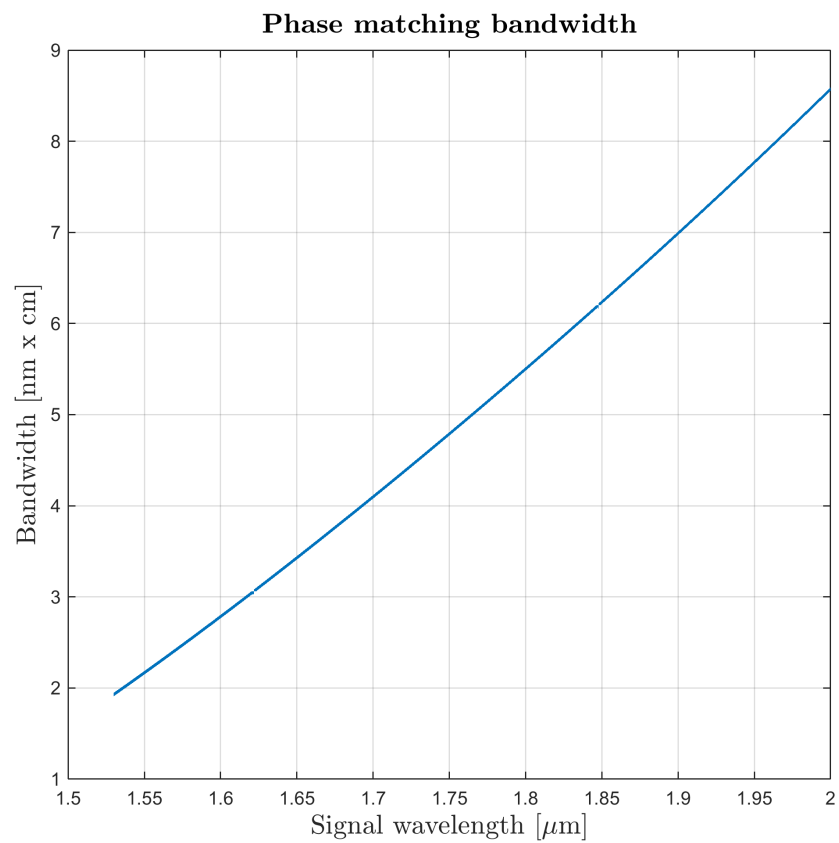
Figure 3.5: Phase matching bandwidth in type IIb phase matched KTA in the xz-plane as a function of signal wavelength. The pump wavelength is fixed at 1053 nm.
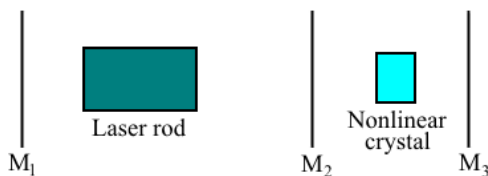
Figure 3.6: Fundamental concept of an IOPO. The OPO resonator formed by mirrors M_2 and M_3 is a part of the laser resonator formed by mirrors M_1 and M_3.

3.4 Dynamics of an intracavity parametric oscillator

The fundamental concept of an IOPO is shown in figure 3.6. The mirrors M_1 and M_3 form the laser resonator, and the mirrors M_2 and M_3 form the OPO resonator with a nonlinear crystal inside. Both mirror M_1 and M_3 are highly reflective at the pump frequency ω_3, so the pump is contained within the resonator. M_3 is chosen to have a suitable output coupling at the signal and the idler frequencies.

The full dynamics of an IOPO is beyond the scope of this text. However, there are some key concepts that come from a qualitative analysis of the system. Assume a Q-switched laser is pumping an IOPO. When the Q-switch opens, the pump pulse starts building in intensity. Conversion does not start until the pump pulse has surpassed the OPO threshold. As the signal output grows in intensity, it starts depleting the pump pulse. With optimal timing, the signal pulse starts when the pump pulse has reached its maximum [14]. At this point, all the energy has been extracted from the laser rod. Rapid pump depletion is desired to avoid damage on components due to the high intensities in the resonator.

If the signal starts too early, it can deplete the pump before it manages to extract all the energy from the laser rod. If there is sufficient energy left in the rod, the process can repeat itself and lead to multiple pulses. This can happen if the nonlinear crystal is too long. If the nonlinear crystal is too short, the signal pulse can start too late and lead to energy being lost to the resonator round trip loss.

Numerical simulations are useful to illustrate several of these phenomena (e.g. [13] and [14]). Multipulsing and inefficient conversion is shown in figure 3.7 for an OPO pump of $1053\,\mathrm{nm}$ and an OPO signal of $1600\,\mathrm{nm}$. The nonlinear crystal is KTA with type IIb phase matching in the xz-plane. In (a), the crystal length is $15\,\mathrm{mm}$ long, in (b) this is reduced to $5\,\mathrm{mm}$.
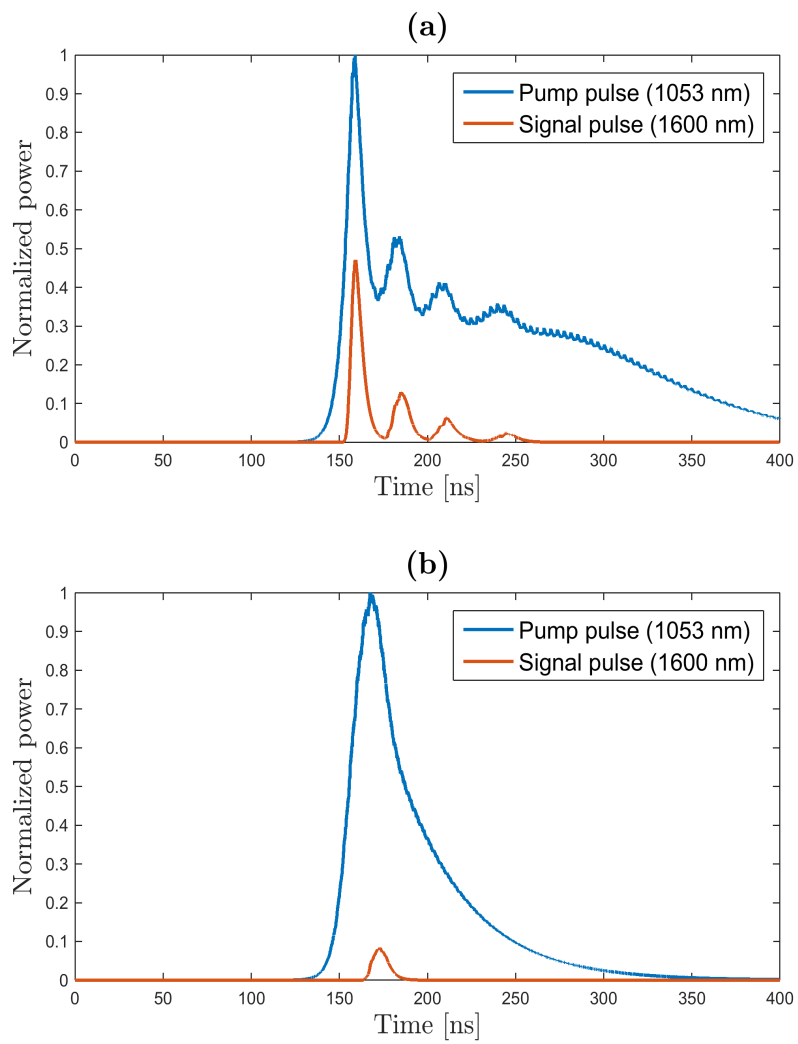
Figure 3.7: Illustration showing multipulsing for a 15 mm long nonlinear crystal (a) and inefficient conversion for a 5 mm long nonlinear crystal (b).

Chapter 4

Computational methods

This chapter will describe a general method for simulating a Q-switched intracavity optical parametric oscillator (IOPO). An IOPO is a fairly complex physical system. It involves the interactions in the laser medium, the nonlinear interactions and thermal effects in the laser rod, and is well suited for computer simulations. For this purpose, a computational model for solving the dynamics of this system will be described in the following sections.

The concept of pumping is used both in the context of the laser diode pumping a laser and a beam pumping an OPO. To avoid confusion, anything referring to pump or pump beams refer to the laser diode pump. The OPO pump coming from the solid state laser will be referred to as the $1\,\mu$m signal. The output from the OPO will be referred to as the $1.6\,\mu$m signal. Any mention of population refers to the population in the upper laser level.

4.1   Simulation software

The simulations uses a combination of two different software. The primary software is SISYFOS (Simulation System for Optical Sciences), a software developed at FFI. It can take into account 3D diffraction with spectral resolution, dispersion, laser media interaction and nonlinear interactions. Sisyfos can simulate various thermal effects of the laser rod, notably a temperature dependent refraction index and end face expansion. The simulations can use several spatial symmetries (cylindrical, half plane, quadrant) as well as run plane wave simulations [29].

Sisyfos implements the thermal effects in different ways depending on the effect. The thermo-optical effect is implemented by introducing a temperature profile in the material and specifying the thermo-optical coefficients. The end face deformation is implemented as two lenses with a given expan-

sion profile and a given refractive index. At the time of writing, photoelastic effects were not implemented in Sisyfos, and these are therefore not included in the simulations.

Sisyfos relies on an external source to supply both temperature profile and displacement data. In the simulations, this is supplied by the finite element method (FEM) software Comsol Multiphysics. Comsol also supplies the values of the thermal stress to compare against the fracture limit to ensure that the structural integrity is preserved. Python was employed to manage the data flow between Sisyfos and Comsol, as well as keeping track of simulation parameters.

4.2 Simulation structure

Our scope is to study the dynamics of a continuously pumped, Q-switched IOPO. To do this, an iterative scheme with repeated pumping and lasing was implemented. The procedure follows a three step iteration that can be summarized in the following points

- Pump simulation. Build up a population inversion and deposit heat (Sisyfos)

- FEM analysis of thermal effects. Find steady state temperature profile, expansion and stress (Comsol)

- Laser simulation. Generate a pulse from the stored population, using a calculated thermal lens (Sisyfos)

After performing these three steps, the process is repeated. This procedure is performed for a given number of iterations, checking for convergence. The goal is to find the steady state solution with stable output.

The justification behind this kind of scheme comes from the dynamics of the system. When the Q-switch is closed, the only dynamic of interest is the storage of energy in the medium (population and heat). This happens over a time scale of $200\,\mu\text{s}$ for a pulse repetition rate of $5\,\text{kHz}$. There is no need for a fine time resolution in this part, as the dynamics are fairly slow. In comparison, the pulse can build up and pass in a time span of 200-500 ns. Splitting the pumping and the pulse allows much better resolution of the pulse without needlessly increasing the computational time.

The heat stored in the pump simulation is used to calculate the corresponding thermal lensing. The data imported to Comsol is the total heat absorbed per unit volume. This is multiplied with the repetition rate to give

the steady state heat generation. The laser rod is assumed to be cylindrical with cooling along the sides. The exterior is assumed to keep a constant temperature of 293 K. Approximately 20-30% of the absorbed pump energy is deposited as heat in the laser rod, depending on the pump wavelength.

The population stored after pumping is used as an initial condition for a pulse simulation. Both the temperature profile and the end face expansion are included in this simulation. The simulation is run until the pulse has passed, or in the case of IOPO simulations when the $1\,\mu$m pulse has dissipated.

After the pulse has passed, the remaining population (if any) is used as an initial condition for a new pump simulation. The thermal effects used for the pulse are included in this simulation to study how the pump distribution changes with thermal lensing. In theory, the inclusion of thermal effects on the pump simulation could lead to an infinite loop where the temperature profile does not stabilize. Fortunately, all configurations tested converged in a rapid manner.

The nonlinear crystal will typically absorb some of the interacting beams, leading to heat dissipation in the crystal. For simplicity, all thermal effects were ignored in the nonlinear crystal. However, these effects could be implemented in a similar manner as the thermal effects in the laser rod.

The simulation can switch between two modes, with or without the IOPO element. When enabling the OPO, the output coupler is simply replaced with a resonator consisting of two mirrors and a nonlinear crystal. In this way, the simulations can switch between simulating with the nonlinear conversion or not.

The pump laser diode is simulated with no bandwidth. This simplifies the pump simulation.When only simulating the $1\,\mu$m signal, this is also done with no bandwidth. However, as the spectral properties of the $1\,\mu$m signal can affect the OPO output, it is not expected that this gives a correct result when performing IOPO simulations. This is corrected by giving the $1\,\mu$m emission cross section a bandwidth (as specified by the material) and running the IOPO simulations with spectral resolution.

The simulations are run with a spatial resolution of $0.1\,$mm. This was found to work well for almost all cases. The pump simulation is run for approximately $200\,\mu$s, and has a time resolution of $1\,\mu$s. The pulse simulation is typically run for a few hundred nanoseconds (250-500 ns). Without the IOPO, the time resolution is the same as the round trip time of the resonator (most cases around 1.5 ns). When simulating with the IOPO, the time resolution is finer (most cases around 0.4 ps).

Chapter 5

Simulation goals and parameters

5.1 Simulation goals

The goal of the simulations is to design and optimize an intracavity optical parametric oscillator with a tunable signal around $1.6\,\mu$m. The IOPO is pumped by a Q-switched, end-pumped Nd:YLF laser with a wavelength of $1053\,$nm.

The desired specifications can be summarized to

- Signal pulse energies of $1\,$mJ or higher when supplied with $30\,$W input power from the pump diodes at $5\,$kHz pulse repetition rates with a wavelength of $1.6\,\mu$m

- A beam quality (M^2) of 2 or better.

- Temporal pulse width equal or less than $10\,$ns.

- Radiant fluences below damage thresholds ($3\,$J/cm^2).

A too high fluence on the nonlinear crystal or laser rod can cause damage to the antireflective coating. Damage threshold for the nonlinear crystal coatings is set to 2-3 J/cm^2. This estimate is a lowered threshold of the threshold given in [30]. This damage threshold is specified for KTP (potassium titanyl phosphate, KTiOPO$_4$), and has a value of $4\,$J/cm^2.

An intracavity OPO was chosen over an extracavity OPO, as IOPOs can potentially reach higher efficiencies than external OPOs [8] and can be made more compact (see f.i. [15]). The disadvantage is that the higher fluences in the resonator can cause damage more easily.

The simulations are split into three parts. The first is to reproduce the results from an IOPO demonstrated by Peng et al. [17]. This is done to ensure our simulation produces sensible results and to calibrate the simulation parameters. Ref. [17] was chosen as it uses the same materials (Nd:YLF and KTA) as well as similar pump power and repetition rates to those specified above. The second section studies sensitivity for variation of some selected parameters. The third focuses on optimizing the design of an IOPO by finding a suitable set of simulation parameters, given the specifications above.

5.2   Choice of materials

The laser rod material chosen for this application is neodymium doped $LiYF_4$ (yttrium lithium fluoride, YLF). YLF has several properties that make it a well suited choice over some of the other alternatives, notably Nd:YAG (yttrium aluminium garnet, $Y_3Al_5O_{12}$) and Nd:YVO$_4$ (yttrium orthovandate). The upper state lifetime of YLF is approximately $480\,\mu$s [31] compared to $250\,\mu$s in YAG [31] and $100\,\mu$s in YVO$_4$. Using a pulse repetition rate of $5\,$kHz (pumping time of approx $200\,\mu$s) makes YVO$_4$ unattractive due to the short lifetime. Compared to YAG, YLF has lower stimulated emission cross section [31], and is YLF is more brittle than YAG. However, the thermal lensing is weaker in YLF [10]. This, along with a higher upper state lifetime favours the choice of YLF.

YLF is a birefringent material, and the lasing wavelength is polarization dependent. The polarization parallel to the crystal axis (π-polarization) has a wavelength of 1047 nm, whereas the polarization orthogonal to the crystal axis (σ-polarization) has a wavelength of 1053 nm. Due to the natural birefringence in the material, there is virtually no issue with thermally induced birefringence [24].

The σ-polarization (1053 nm) was chosen for lasing. While having lower stimulated emission cross section, the thermal lensing is also lower for this polarization. The π-line can be blocked from oscillating by insertion of a polarizer in the resonator that blocks this polarization.

The most relevant material data for Nd:YLF are listed in table 5.1. Data from [11, 31, 32]. Some of the values are polarization-dependent or vary between axes.

Table 5.1: YLF material properties

Lasing wavelength	1047 nm (π)
	1053 nm (σ)
Thermo-optic coeff.	-4.3 ppm/K (π)
	-2 ppm/K (σ)
Emission cross section	$3.7 \cdot 10^{-19}$ cm^2 (π)
	$2.6 \cdot 10^{-19}$ cm^2 (σ)
Lasing linewidth	14.5 cm^{-1} (π)
	12.5 cm^{-1} (σ)
Linear expansion coeff.	8 ppm/K ($\parallel$ c-axis)
	13 ppm/K ($\perp$ c-axis)
Upper state lifetime	480 μs
Density	3.95 g/cm^3
Thermal conductivity	6 W/mK
Ultimate tensile strength	40 MPa
Young's Modulus	$7.65 \cdot 10^9$ kg/m^2
Poisson's ratio	0.33
Upconversion rate	$17 \cdot 10^{-17}$ cm^3/s
Refractive index (1064 nm)	1.46

Table 5.2: KTA material properties

Point group	mm2
Density	3.454 g/cm^3
Refractive index (1053 nm)	1.868 (z)
	1.793 (y)
	1.789 (x)
Nonlinear coefficient	2.5 pm/V (d_{15})
	4.5 pm/V (d_{24})
	2.8 pm/V (d_{31})
	4.2 pm/V (d_{32})
	16.2 pm/V (d_{33})

The nonlinear crystal is chosen to be KTA (potassium titanyl arsenate, KTiOAsO$_4$). Compared to a similar material like KTP it has a higher damage threshold [33] and better IR-transparency (figure B.1, [34]). The simulations will employ a type IIb phase matching with propagation in the xz-plane. The phase matching properties (phase matching angles, effective nonlinearity and phase matching bandwidth) for this phase matching type can be found in figure 3.3, 3.4 and 3.5. Some material properties are listed in table 5.2, data from [28].
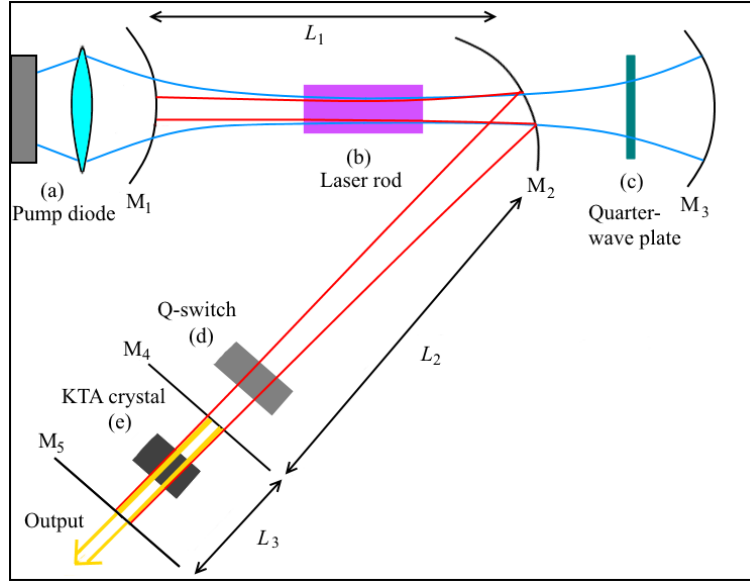
Figure 5.1: Resonator design. Main components labelled (a)-(e), mirrors M_1-M_5 and resonator dimensions $L_1 - L_3$. The pump is shown in blue, the $1\,\mu$m signal in red and the $1.6\,\mu$m signal in yellow.

5.3 Resonator design and simulation parameters

An illustration of the resonator design is shown in figure 5.1. The pump profile (blue), $1\,\mu$m signal profile (red) and the $1.6\,\mu$m signal (yellow) are illustrated. The main components are labelled (a)-(e), and are given as follows: (a) pump diode and focusing element, (b) laser rod, (c) quarter wave plate, (d) modulator, (e) KTA crystal.

The mirrors are labelled M_1-M_5, and are summarized in table 5.3. The mirrors are denoted by their reflectivity, being highly reflecting (HR), partially reflecting (PR) and anti-reflecting (AR). The resonator lengths are labelled $L_1 - L_3$. L_1 is the total length between mirrors M_1 and M_2, L_2 is the total length between mirrors M_2 and M_4 and L_3 is the total length between mirrors M_4 and M_5 (OPO resonator length).

The folding mirror M_2 has two primary purposes. It splits the resonator into two arms. This separates the pump and laser signal paths as the pump continues to M_3. It also acts as a focusing element, focusing the beam towards the mirror M_4 and the nonlinear crystal. In the simulations, the mirror M_2 is placed very close to the laser rod.
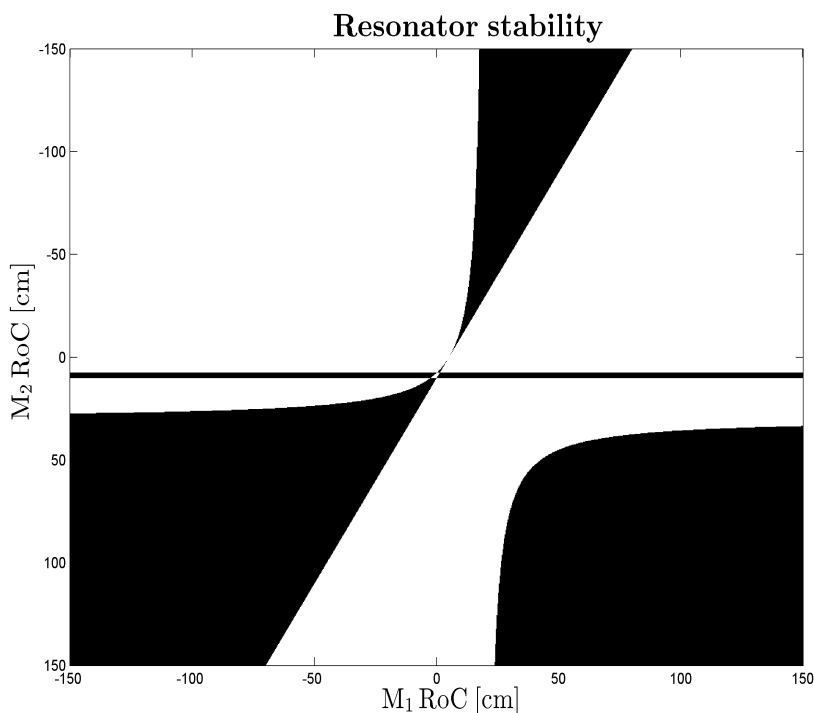
33

Figure 5.2: Stability diagram for resonator in figure 5.1. This is shown for variations in the radius of curvatures of mirrors M_1 and M_2 with a fixed resonator length. The areas in black are stable, with the areas in white unstable.

The pump enters through mirror M_1 and is focused in the center of the laser rod with a suitable focusing element. The pump mirror M_3 reflects the pump beam back for another pass through the crystal. The radius of curvature of the mirror is chosen to match the pump beam curvature (2.7) so the pump beam retraces itself on the return pass. The spacing between the pump mirror and the folding mirror M_2 is taken to be a few centimetres.

A stability diagram for the resonator found from (2.14) is shown in figure 5.2. This is shown for variations in the curvature of the mirrors M_1 and M_2. This is found for $L_1 = 6\,\mathrm{cm}$ and $L_2 + L_3 = 15\,\mathrm{cm}$ for no thermal lensing. The areas marked in black are stable, with the areas in white unstable.

Absorption in YLF is polarization dependent. The pump light emitted from the pump diodes is assumed to be equally split in two polarization states. To ensure good absorption, a quarter wave plate (ref (c) in figure 5.1) is inserted. This wave plate swaps the polarization state of the pump on the return pass, resulting in equal absorption of both polarizations.

Table 5.3: Resonator mirrors

Mirror	Radius of curvature	Reflectivity
M_1	Adjustable	HR at 1053 nm
		AR at 808/877 nm
M_2	Adjustable	HR at 1053 nm
		AR at 808/877 nm
M_3	Adjustable	HR at 808/877 nm
M_4	Plane	AR at 1053 nm
		HR at $\sim$1600 nm
M_5	Plane	HR at 1053 nm
		PR at $\sim$1600 nm

Table 5.4: Absorption cross sections in Nd:YLF

Wavelength (nm)	Polarization	Cross section (cm^2)
808	π	$9.15 \cdot 10^{-21}$
	σ	$1.39 \cdot 10^{-20}$
877	π	$3.03 \cdot 10^{-21}$
	σ	$2.79 \cdot 10^{-21}$

The pump is a fiber coupled laser diode with a wavelength of 808 nm or 877 nm. The maximum output power of the pump is 30 W and the beam quality is $M_P^2 \approx 40$ [35]. The absorption cross sections for these wavelengths were found from absorption measurements at FFI [35]. They are listed in table 5.4. The absorption measurements are shown in figure B.2.

5.4 Parameter uncertainty

Some simulation parameters are hard to estimate accurately or vary between sources in the literature. One example is the resonator round trip loss. This is seldom known to high accuracy. The value of this parameter strongly affects the output power of the laser as well as the fluences in the resonator. An estimate for the loss can be found by making an estimate for each component and summing up to a total loss.

Some sources [12, 36] specifies two values for the thermal conductivity in YLF, either along the crystal axis (7 W/mK) or perpendicular to this axis (5.3 W/mK). Other references [24, 31, 32] specify one value of 6 W/mK, which is the value used in the simulations. This value seem to be some sort of compromise between the two values.

The thermo-optical coefficient is crucial to determine the thermal lensing. There exists at least two different values for the thermo-optical coefficients in the literature. The values listed in table 5.1 are tabulated in [31], but a different set of values are given by Aggarwal et al. [36]. They cite values of -4.6 ppm/K and -6.6 ppm/K for σ- and π-polarization respectively. An incorrect value of this parameter could make an otherwise stable resonator unstable (or vice versa).

The value for the upconversion rate is not certain. The value listed in table 5.1 ($17 \cdot 10^{-17}$ cm^3/s) comes from Clarkson [11], but this rate might change with doping concentration [37]. This dependence on the doping is assumed to stem from clustering of dopant ions at higher doping concentrations.

Chapter 6

Simulation Results

This chapter is split in three sections. The first is a comparison between the simulations and results from a similar IOPO. Then follows a brief look at parameter sensitivity for some given parameters. The last part is an optimization based on the resonator described in the previous chapter. This section is further split into two parts. The first optimizes the $1\,\mu$m signal, the second uses these results to optimize the IOPO design with the specifications given in the previous chapter.

6.1 Comparison of simulations to experimental results

To validate the computational model used, it was compared to experimental results. The model was compared to a similar design done by Peng et al. [17]. They use a diode pumped, Q-switched Nd:YLF laser with a KTA IOPO to generate a signal around $1.9\,\mu$m, using a resonator similar to the one shown in figure 5.1.

Peng et al. have results for both a pure $1\,\mu$m signal as well as IOPO signal output ($1.9\,\mu$m signal). The results from the article are listed in table 6.1. Included in this are the average output power of the pure $1\,\mu$m signal and pulse energies for the $1.9\,\mu$m signal at fixed repetition rates. All results are stated for a pump power of $36\,$W. There is no mention of beam quality besides a value of 1.1 for the $1\,\mu$m signal output.

The pump diode beam quality is estimated to be $M_P^2 \sim 300$ from values stated in the article. For the $1\,\mu$m signal, the round trip loss was estimated to be 5%. This value was found by assuming a 0.5% loss in each component per pass. When using the IOPO, the round trip loss was set to 10%.

Table 6.1: Peng et al. results

Rep.rate (kHz)	1 μm output (W)	1.9 μm pulse energies (mJ)
1	6.5	2.5
2	9.2	1.55
4.5	11.6	0.67

Table 6.2: Simulation results

Rep.rate (kHz)	1 μm output (W)	1.9 μm pulse energies (mJ)
1	6.15	2.25
2	9	1.38
4.5	10.85	0.68

The simulation results are listed in table 6.2. The simulations gave a beam quality of approximately 1.2 for the 1 μm signal and 3.5 for the 1.9 μm signal.

In the simulation, the 1.9 μm signal pulse widths were approximately 6 ns (FWHM) for all repetition rates. The entire pulse passes in ∼20 ns. The simulations gave a total fluence in front of the KTA crystal of 15 J/cm^2 for 1 kHz repetition rate, with a reduction to 8-9 J/cm^2 for 4.5 kHz. Double pulsing is also seen for a repetition rate of 1 kHz.

6.2 Parameter sensitivity

This section gives a brief look on parameter sensitivity in the simulations. Three parameters are tested, the round trip loss, the thermo-optical coefficient and the upconversion rate. In addition to this, the effects of the thermal lensing is investigated by removing the thermal lensing completely.

All simulations in this section are simulations of the 1 μm signal and use a 3 cm long, 1 at.% doped rod pumped with a wavelength of 877 nm. The pulse repetition rate is 5 kHz and the internal round trip loss is set to 10%. Other simulation parameters are found in table 6.3.

To demonstrate the effects of thermal lensing on the system, s simulation with all thermal lensing removed was compared to a simulation with thermal lensing included. The simulation without thermal lensing gave an average output power of 11.8 W with a beam quality of approximately 1.02. The simulation with thermal lensing gave an average output power of 12 W with a beam quality of 1.3. The $1/e^2$-radius for some specific positions in
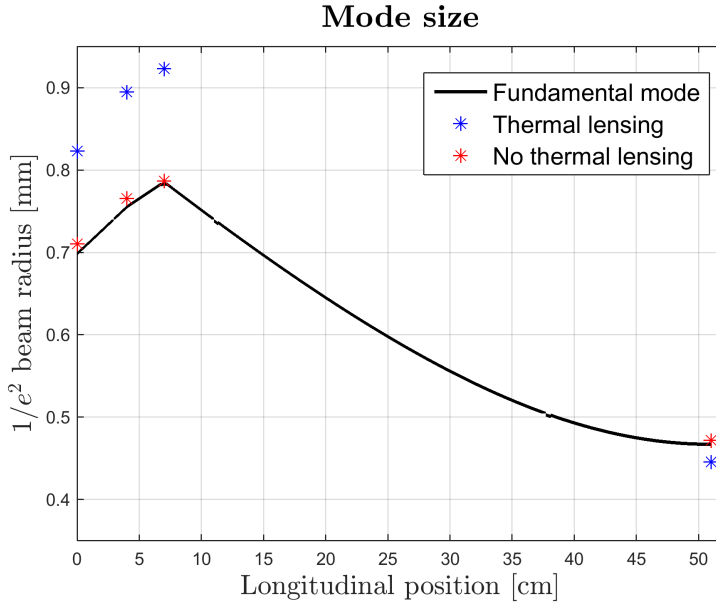
Figure 6.1: Beam size comparison of the $1/e^2$-radius with and without thermal lensing to the fundamental mode.

the resonator of the two cases are shown in figure 6.1. It also shows the fundamental mode found from (2.13).

Next, the round trip loss was altered from its initial value of 10% down to 0. The output power increased from 12 W with 10% loss to approximately 15.9 W for no loss. The maximum fluence at the output coupling also increased with lower losses, from a value of 7.9 J/cm^2 up to 10.5 J/cm^2 for no loss.

To test the dependence on the thermo-optical coefficients, two differing values were compared to see their effect on the output. The two values tested were -2 ppm/K [31] and -4.6 ppm/K [36]. The output had an average power of 12 W and 6 W with a beam quality of 1.3 and 3.6 for the values of -2 ppm/K and -4.6 ppm/K respectively.

The last parameter tested was the upconversion rate. The simulations done compared no upconversion with the value listed in table 5.1[1]. Including the upconversion resulted in a 5-6% increase in the heat dissipated in the laser rod. The output power dropped from 12.2 W to 12 W. Both simulations had a beam quality of approx. 1.3.

---

[1]17·10^{-17} cm^3/s, ref. [11]

Table 6.3: Section 6.2 simulation parameters

L_1	7 cm
L_2	44 cm
M_1 RoC	-50 cm
M_2 RoC	60 cm
OC	30%
r_p (e^{-2})	0.5 mm

6.3 Optimization of IOPO design

The last section focuses on finding an optimized IOPO design. This is split in two parts. The first part will focus solely on optimizing the resonator for optimal output of the 1 μm signal. The second includes an intracavity OPO and focuses on the 1.6 μm signal output.

Unless stated otherwise, the pulse repetition rate is set to 5 kHz, the round trip loss to 10% and the input power to 30 W. The laser rod can vary in length and doping percentage, but it is assumed to be cylindrical with a diameter of 4 mm. Pump radius is defined as the e^{-2}-radius of the beam at focus.

6.3.1 1 μm signal optimization

To make the resonator relatively compact, the length of the second arm formed by mirror M_2 and the OPO was limited to 15 cm. For the simulations without the OPO, this sets L_2 to 15 cm.

The rod was chosen to be 3 cm long with an 1% doping concentration. This is pumped with a wavelength of 877 nm. This gives an absorption that is greater than 90%. The thermal stresses never surpassed 6.5 MPa (von Mises stress) for a pump power of 30 W. An output coupling of 30% was found to be optimal when the round trip loss was set to 10%.

A pump wavelength of 808 nm was also tested. For this pump wavelength, the doping concentration was lowered to 0.5%. In comparison to the 3 cm, 1% doped, 877 nm pumped rod, a 2 cm long, 0.5% doped, 808 nm pumped rod produced roughly the same average output power ($\sim$12 W). The rod pumped with 808 nm had slightly worse beam quality (1.5 versus 1.3) and the maximum thermal stress reached approximately 12 MPa.

Contour plots showing variations in output power, maximum total fluence at the output coupler and beam quality (M^2) are shown in figure 6.2 for variations in the pump radius and the radius of curvature of the mirror M_2. Other simulation parameters are found in table 6.4.

Table 6.4: 1 μm optimization simulation parameters

L1	6 cm
L2	15 cm
M1 RoC	-50 cm
OC	30%

The maximum output power in figure 6.2 (a) is estimated to occur for a curvature R of 75 cm and a pump radius r_p of 0.35 mm. An input/output (IO) curve for these specific parameters is shown in figure 6.3. This is labelled case 1. It also includes a curve for the values used in the IOPO simulations (next section). This is labelled case 2. Here, $R = 86$ cm and $r_p = 0.5$ mm.
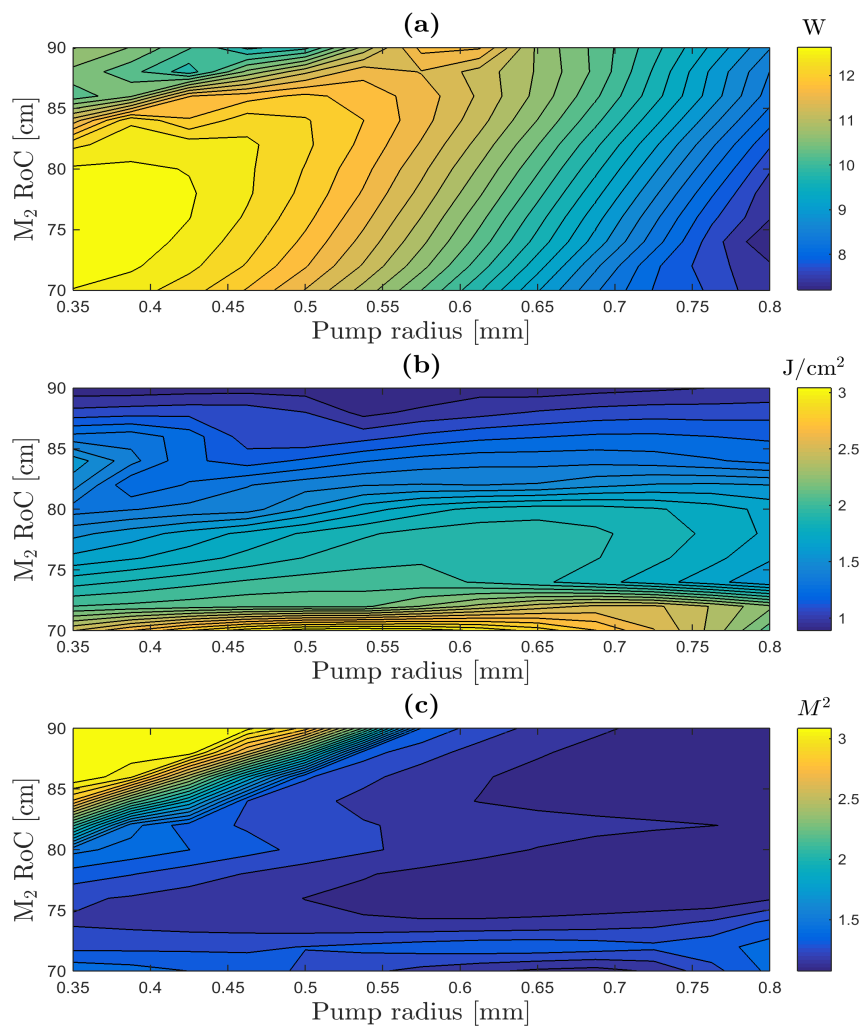
Figure 6.2: Contour plots of output power (a), maximum total fluence at the output coupler (b) and beam quality M^2 (c) for variations in the radius of curvature and pump radius.
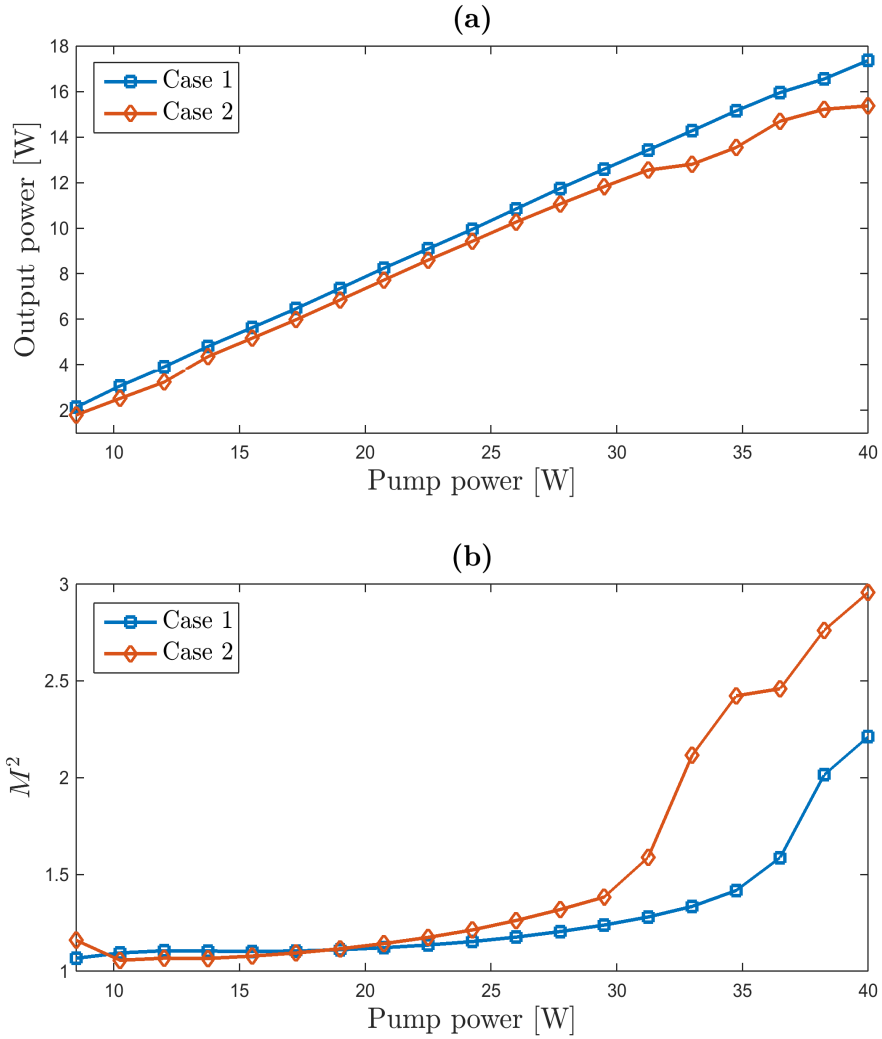
(a)

(b)

Figure 6.3: IO-curve showing output power (a) and beam quality M^2 (b) for two specific choices of pump radius r_p and M_2 curvature R. Case 1 corresponds to $r_p = 0.35\,\mathrm{mm}$ and $R = 75\,\mathrm{cm}$, and case 2 to $r_p = 0.5\,\mathrm{mm}$ and $R = 86\,\mathrm{cm}$
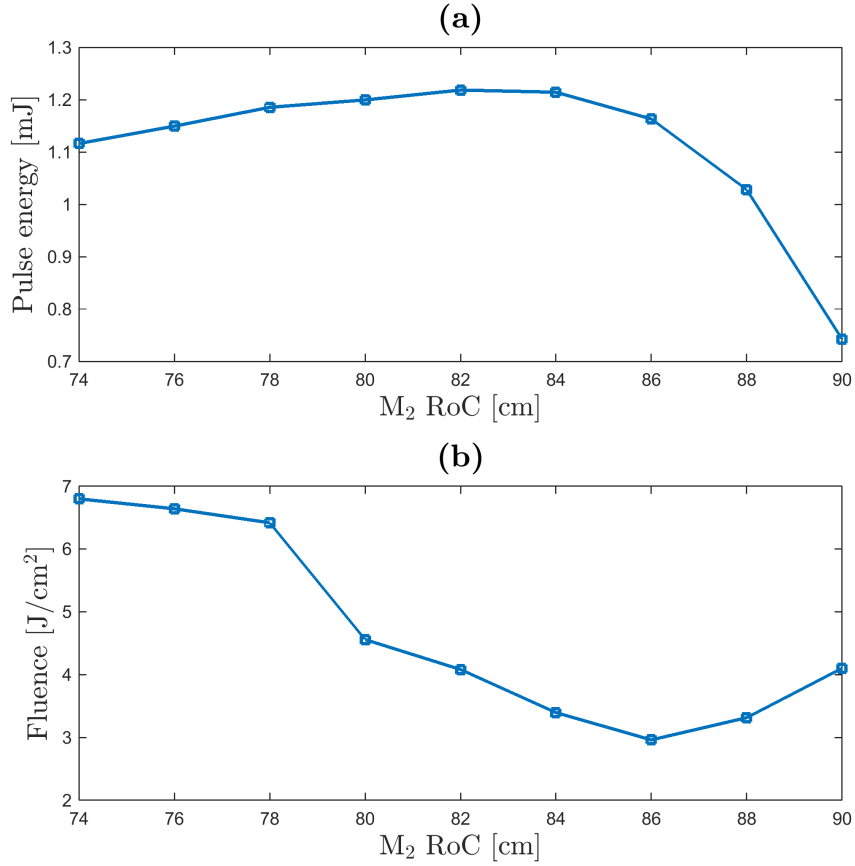
Figure 6.4: Average pulse energy of the 1.6 μm signal (a) and maximum total fluence at the KTA crystal (b) for varying radius of curvature of the mirror M_2.

6.3.2 IOPO optimization

When simulating with the IOPO, the length of L_2 was reduced to 12 cm with an OPO length L_3 of approximately 3 cm. This keeps the total arm length between M_2 and M_5 fixed at 15 cm.

Including the IOPO caused the fluences in the system to increase. This is seen in figure 6.4, where the pulse energy of the 1.6 μm signal and maximum total fluence in front on the KTA crystal is illustrated for varying radius of curvature of the mirror M_2. Other simulation parameters are found in table 6.5. For a value of 75 cm, the fluence reached values of 6-7 J/cm^2, which surpasses the damage threshold (3 J/cm^2). A value of 86 cm was chosen for the radius of curvature in order to get below the damage threshold.

Table 6.5: IOPO simulation parameters

L_1	$6\,\mathrm{cm}$
L_2	$12\,\mathrm{cm}$
L_3	$3 \pm 0.3\,\mathrm{cm}$
M_1 RoC	$-50\,\mathrm{cm}$
M_2 RoC	$86\,\mathrm{cm}$
OC ($1.6\,\mu\mathrm{m}$)	50%
OC (idler)	100%
$r_p\ (e^{-2})$	$0.5\,\mathrm{mm}$

The design was further tested for variations in the KTA crystal length. The KTA crystal length was varied from 8 to 13 mm. An important consideration here is to avoid double pulsing. Other simulation parameters are found in table 6.5. The results are shown in figure 6.5 for pulse energy, maximum total fluence (at the KTA crystal) and beam quality. No double pulsing was observed for any of the crystals lengths tested in this simulation.

From these results, a value of 10 mm was chosen considering all three parameters shown in figure 6.5. The pulse shape for this specific value is seen in figure 6.6. It shows the signal pulse with the corresponding $1\,\mu\mathrm{m}$ pump pulse. The average pulse energy is 1.16 mJ with a beam quality of approximately 2. The pulse width is 3.6 ns (FWHM), with the entire pulse passing in 15 ns. In addition to this, the OPO generated an idler with a wavelength of $3.08\,\mu\mathrm{m}$ and 0.42 mJ average pulse energy.

Field distributions for the total near field and total far field of both the $1\,\mu\mathrm{m}$ and $1.6\,\mu\mathrm{m}$ signal are shown in figure 6.7. Fields (a)-(b) are the total near/far field of the $1\,\mu\mathrm{m}$ signal at the front of the KTA crystal. The fields (c)-(d) are similarly the $1.6\,\mu\mathrm{m}$ fields at the output coupler M_5. The wavelength spectrum of the signal and idler is shown in figure 6.8. The FWHM bandwidth of the $1.6\,\mu\mathrm{m}$ signal is estimated to 1-1.5 nm and approximately 5 nm for the idler.

To demonstrate the ability to tune signal wavelength, the simulations were run with a varying signal wavelength. The resulting change in phase matching angle and effective nonlinearity can then be found from figure 3.3 and 3.4. The pulse energies for varying signal wavelength are shown in figure 6.9.
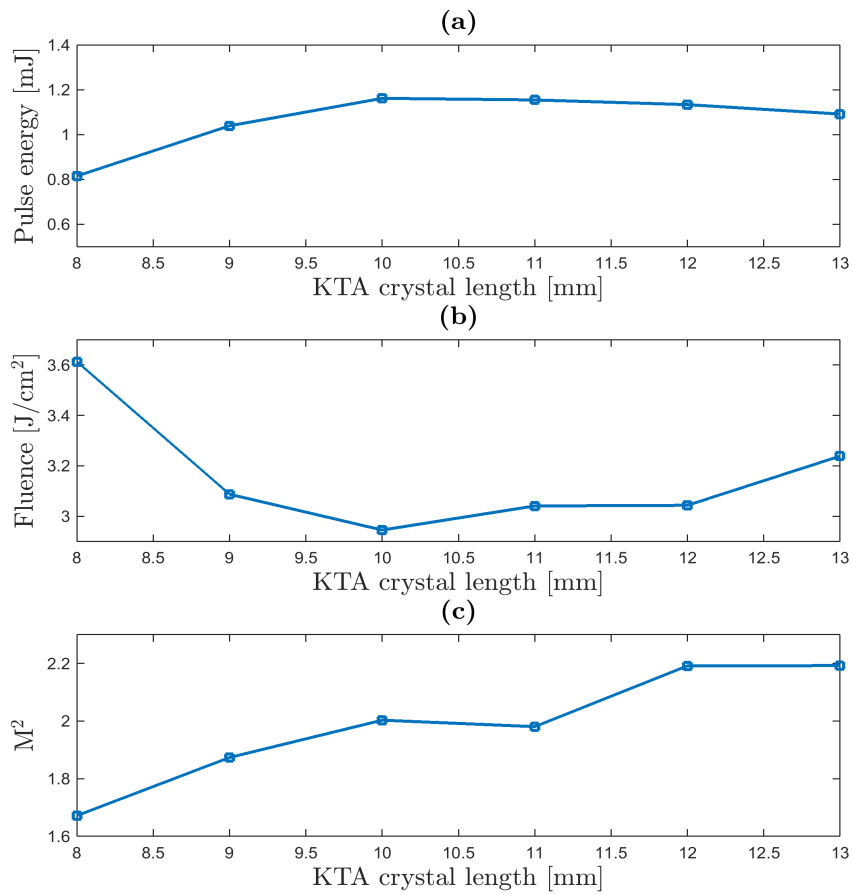
Figure 6.5: Average pulse energy (a), maximum total fluence at the KTA crystal (b) and beam quality (c) as a function of KTA crystal length for the 1.6 μm signal.
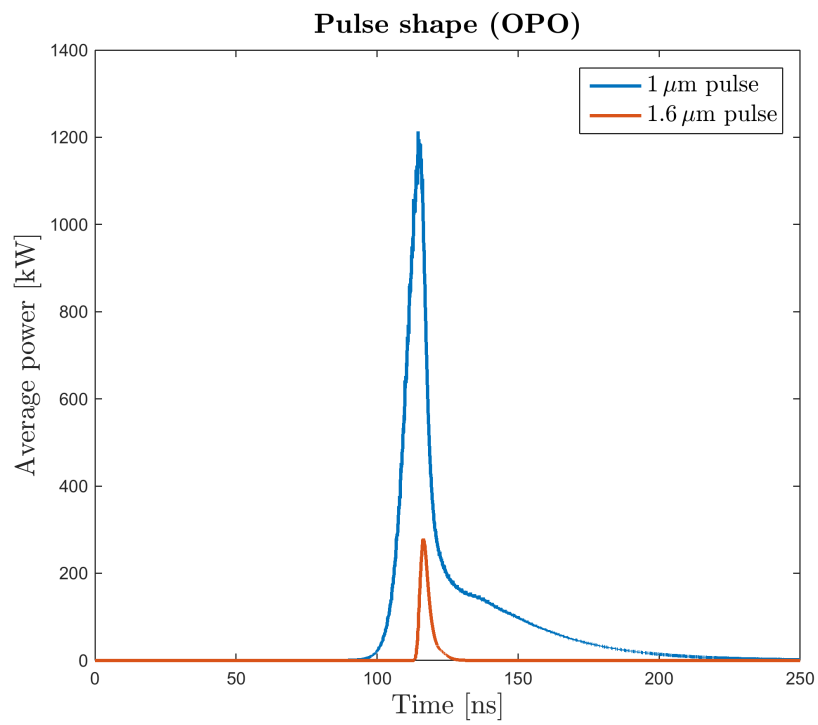
Figure 6.6: Pulse shapes, showing both the $1\,\mu$m pulse and the $1.6\,\mu$m signal pulse. The pulses have been smoothed by a low pass filter.
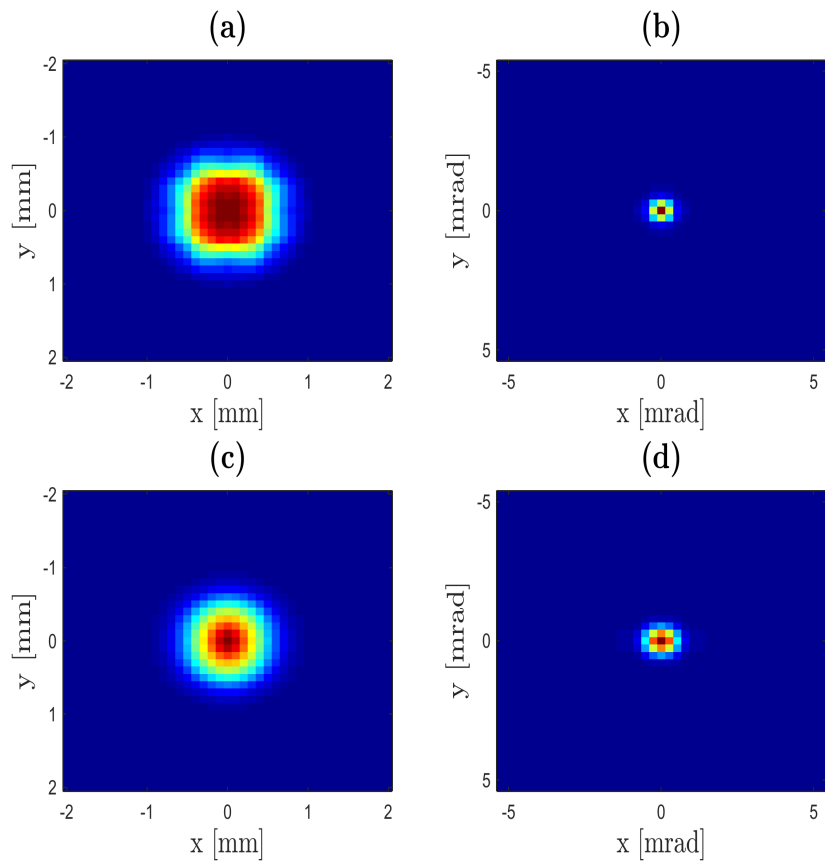
Figure 6.7: Figure showing total near field and total far field of the 1 μm signal at the KTA crystal (a-b) and total near field and total far field of the 1.6 μm signal at the output coupler M$_5$ (c-d).
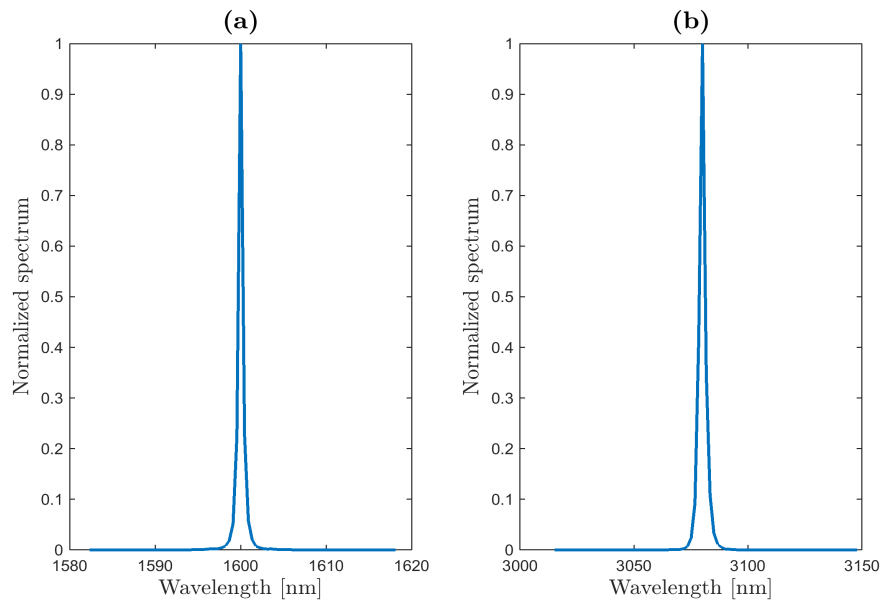
Figure 6.8: Wavelength spectrum of $1.6\,\mu$m signal (a) and idler (b).
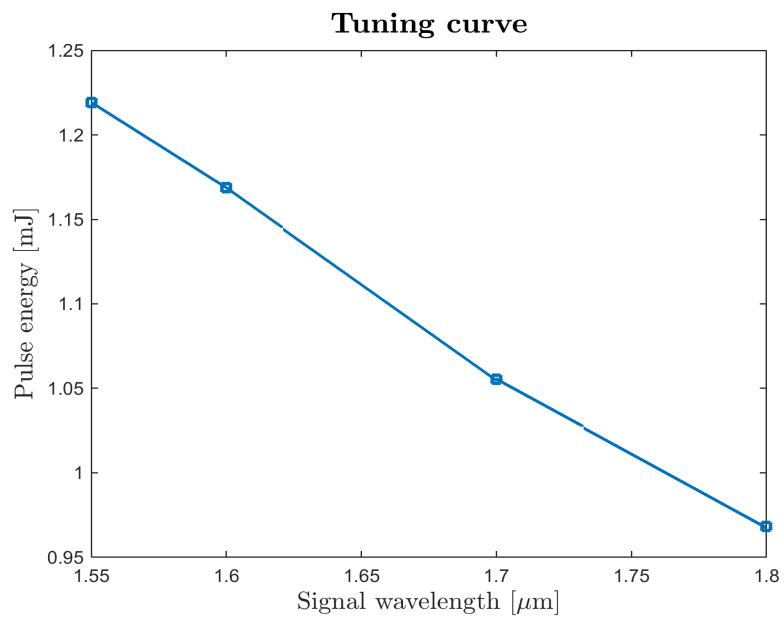

Figure 6.9: Tuning curve showing variations in pulse energies for varying IOPO signal wavelength.

Chapter 7

Discussion and conclusion

7.1 Comparison of simulations to experimental results

The simulations started out with a test of the computational model with experimental results. This was done to check the correspondence between simulated results and actual experiments. Peng et al. [17] was chosen as they used a combination of YLF and KTA. The design of the resonator was to some extent motivated by their design.

One thing that did not match the article was the type of phase matching. Peng et al. specifies phase matching in the yz-plane in their article, but it was found that the conversion in this phase matching type was too low. It was therefore judged that the actual results had used type IIb phase matching in the xz-plane as this gives the highest nonlinear coefficient.

As mentioned in the previous chapter, Peng et al. have both results for a pure $1\,\mu$m signal and for a $1.9\,\mu$m signal from an IOPO. For the $1\,\mu$m signal, they report average output powers of 6.5, 9.2 and 11.6 W for fixed repetition rates of 1, 2 and 4.5 kHz. The simulation results are 6.15, 9 and 10.85 W respectively. This difference could simply be attributed to a too high estimate for the round trip loss used in the simulations.

For the IOPO, Peng et al. specifies $1.9\,\mu$m signal pulse energies of 2.5, 1.55 and 0.67 mJ for the same repetition rates. The simulation results are 2.25, 1.38 and 0.68 mJ. Peng et al. states that they get double pulsing for a repetition rate of 1 kHz, and this is also seen in the simulations.

The difference in IOPO pulse energies cannot be explained by the round trip loss alone. The simulation pulse energies are lower for 1 and 2 kHz, but higher for 4.5 kHz. In the article, the pulse energies die off when the repetition rate is set even higher (ref. figure 6 in [17]). This does not seem

to be the case for the simulations. One indication of this is seen in the pulse durations. Peng et al. states values of 10, 15 and 41 ns for pulse widths (1 kHz, 2 kHz and 4.5 kHz respectively). The simulations produced a FWHM pulse width of 6 ns for all repetition rates. The cause of this discrepancy is unclear.

Another serious concern are the fluences in the simulations. The article does not mention any numbers relating to the fluences, but the values from the simulations are higher than what is expected to cause damage on components. The lowest value obtained was approximately 8-9 J/cm^2, almost three times the value considered as the damage threshold. Peng et al. only mentions coating damage when generating a signal with a wavelength of 1.6 μm. This damage is attributed to idler absorption in water. The high fluences might be a result of the remaining pump after the signal pulse has passed.

7.2 Parameter sensitivity

One of the advantages with computer simulations is that they allow for rapid testing of various parameters. Included in the results was a brief look on parameter sensitivity on some specific parameters. There are numerous parameters that could be tested, but time limitations hindered more extensive testing.

A high round trip loss reduces the pulse energies from the laser as well as the fluences in the resonator. Going from a lossless resonator to a 10% round trip loss reduced the average output power by almost 25%. Meanwhile, the fluences in the resonator decreased correspondingly by 25%. While a low loss is usually beneficial, it might be an advantage to include some loss in applications where it is important to avoid component damage. This way, the application can sacrifice pulse energy to avoid damage.

An important goal was to include the thermal lensing in the simulations. The exact influence of the thermal lensing is seen in figure 6.1. Without the thermal lensing, the beam width is seen to fit very well with the theoretical mode size in the resonator. When the thermal lensing is included, the mode profile is altered. The beam quality deteriorates slightly from 1.02 to 1.3. This is most likely cause by the aberrations of the thermal lens. The average output power increases slightly (1.7%), which is likely a result of a slightly better overlap between the pump and the signal in the laser rod (positioned between 4-7 cm mark in figure 6.1).

An important part of determining the strength of the thermal lensing is the thermo-optical coefficient ($\mathrm{d}n/\mathrm{d}T$). The case of YLF is somewhat special as the thermo optical coefficient is negative. This means that the end face

expansion and thermo-optical effect will counteract each other. Two different values found in the literature was tested (-2 ppm/K and -4.6 ppm/K). The simulations with the strongest thermal lensing (-4.6 ppm/K) had the pulse energies halved, with a notable deterioration in beam quality (from 1.3 to 3.6). A possible explanation is that the resonator becomes unstable due to the increased negative lens.

One problem with the thermal lens implemented is the lack of photoelastic effects. This could not be implemented as Sisyfos did not support it. There might be reason to believe this effect contributes to the thermal lensing [11]. One estimate of the effect is given by Zelenogorskii and Khazanov [12]. They calculated the relative contributions to the thermal lensing for the three major contributions (thermo-optical, photoelastic, end face expansion) in uniformly pumped Nd:YLF, using experimental data to estimate the photoelastic coefficients. The relative contributions to the optical power of the thermal lens were approximately -2 from the thermo-optical effect, 0.5 from end face expansion and 1.3 from the photoelastic effect[1]. If the contributions are similar for an end-pumped rod, this would indicate that a sizeable positive contribution is missing in the simulations.

Removing the upconversion did not alter the output in any significant way, with a mere 1.5% drop in average output power. Including upconversion resulted in a 5-6% increase in the dissipated heat. This is in contrast to what is stated in the literature [11, 37], where upconversion is mentioned as a potential problem in Nd:YLF. One possible explanation is that the low absorption spreads the population inversion throughout the rod. This lowers the local population inversion and helps reduce the upconversion processes. It could also be that the rate found in the literature is too low, or that the rate used in Sisyfos does not accurately model the issues with high doping concentrations.

It was also discovered that the value for the stimulated emission cross section used in the simulation might be too high. The value listed in table 5.1 ($2.6 \cdot 10^{-19}$ cm^2) was used in the simulations. Other sources set this to around a factor 2 lower [24, 37] (1.2-$1.4 \cdot 10^{-19}$ cm^2). As the stimulated emission cross section affects the pulse build up time and extraction of stored energy, it might favour a different values for parameters such as the output coupling and pump radius.

---

[1]All these numbers apply for a σ-polarized wave

7.3 IOPO optimization

The main goal with the computational model was to use it to optimize the design of an IOPO with a set of given specifications (listed in section 5.1). The resonator used was inspired by Peng et al. [17], but with some modifications. The simulations used double pass pumping instead of two separate pump diodes, and the resonator was overall shorter. The decision to make it shorter was motivated by having a compact design.

As the OPO is pumped by the $1\,\mu$m signal, it was natural to start optimizing this signal to get a good overall efficiency. Due to the numerous simulation parameters available for testing, it was decided to narrow down the scope to a few parameters. In particular, the simulations studied the effect of varying the curvature of the focusing mirror M_2 and the pump radius r_p. These results are summarized in figure 6.2.

For the pure $1\,\mu$m signal, the highest output power seems to be located at a radius of curvature of 75 cm with a pump radius of 0.35 mm. This is case 1 in the IO curve seen in figure 6.3. Here, the effects of the thermal lensing is seen clearly as the beam quality starts to degrade when the pump power increases.

To further describe the behaviour seen in the contour plots, an illustration of the theoretical modes (found from equation (2.13)) for varying curvature of the mirror M_2 is shown in figure 7.1. The position of the laser rod is marked in black. As the curvature increases, so does the fundamental mode size in the resonator. To get good overlap between the laser rod and the mode, a higher curvature should favour a larger pump radius. This is also seen in the contour plot (figure 6.2 (a)).

Another thing to note is that by increasing the curvature, the mode size at the output coupler (and correspondingly, the KTA crystal for the case of an IOPO) increases. This increase in beam width reduces the fluence, which is both seen in figure 6.2 (b) for the pure $1\,\mu$m signal as well as in figure 6.4 for the IOPO. In the latter, the slight increase at the end is caused by a spike in the middle of the transversal profile of the beam.

The choice of pump radius and radius of curvature of mirror M_2 (0.5 mm, 86 cm) was motivated by the reduction of the fluences in the resonator. As seen in figure 6.4, the damage threshold is surpassed for all values with the exception of 86 cm. The pump radius was chosen in an attempt to maximize the $1\,\mu$m signal power. A smaller pump radius could lead to a degradation of the $1\,\mu$m power and beam quality, which in turn deteriorates the $1.6\,\mu$m signal. A larger pump radius could also start reducing the $1\,\mu$m signal power, leading to a lower overall efficiency.
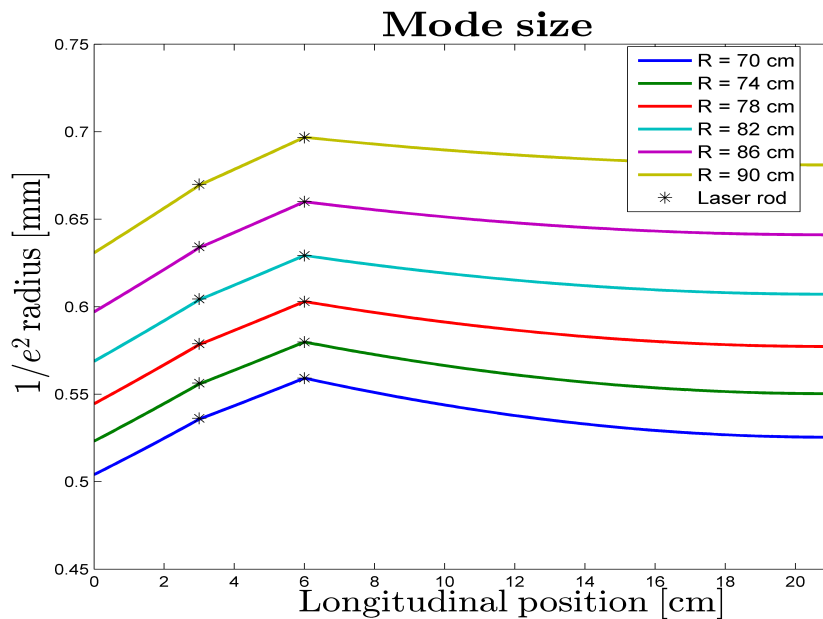
Figure 7.1: $1/e^2$ mode size in resonator with varying radius of curvature R of mirror M_2.

The downside with this choice is the sensitivity to thermal lensing and small parameter changes. The sensitivity to thermal lensing is seen in figure 6.3. As the input power increases over 30 W, the beam quality rapidly deteriorates. This is also seen in the output power, as the efficiency starts to drop when the the pump power grows.

The sensitivity is also seen in the stability diagram for the resonator (figure 5.2). The choices of curvature (M_1 -50 cm and M_2 86 cm) is close to the edge between a stable and an unstable resonator. A negative thermal lens can then bring the resonator even closer to the edge. The lacking photoelastic effect could possibly help reduce the instability if it contributes with a positive sign (ref. [12]).

In hindsight, it might have been favourable to drop the 1 μm even more by increasing the pump radius slightly (f.i. to a value of 0.55 mm). This way, one could hope to reduce the instability in the system while still keeping a decent pulse energy and beam quality. However, time did not allow for the simulations to be repeated with this pump radius.

The simulations with variations in KTA crystal length (figure 6.5) seems to behave in accordance to theory. When the crystal is too short, the conversion takes too long and energy is lost to the round trip loss. If the pulse

is too long, the conversion starts too fast, and the $1\,\mu$m pulse is depleted before it can drain all the energy from the laser rod. In this particular case, the remaining energy is not high enough to generate a new pulse. For this particular set of parameters, the optimal point is found to be 10 mm.

The phase matching bandwidth seems to be a bit smaller than what is expected from the one in figure 3.5. The bandwidth estimated from the figure is roughly 2.5-3 nm (for a 10 mm long crystal) in comparison to the simulation value of approximately 1-1.5 nm. This difference might be investigated more with a finer spectral resolution in the simulations.

As seen in the wavelength tuning curve (figure 6.9), the pulse energies drop as the signal wavelength increase. This can be explained by the reduction of the effective nonlinearity (figure 3.4) for increasing signal wavelengths. The reduced effective nonlinearity decrease the conversion efficiency. A higher signal wavelength might require a slightly longer crystal to compensate.

One issue that was briefly mentioned in the previous chapter was the choice of rod and pump wavelength. A pump wavelength of 808 nm was also an option. This wavelength had higher absorption (ref. table 5.3) than 877 nm. This allows for a lower doping concentration and shorter rods. Pumping a 2 cm long, 0.5% doped rod with 808 nm gives the same, if not higher, absorption than for the rod used (3 cm, 1% doped). However, the output is generally not better than 877 nm as long as there is sufficient absorption in the latter. The thermal stresses are also noticeably higher (around a factor 2) in the 808 nm pumped rod, which is probably caused by the higher quantum defect at 808 nm. Pumping with 808 nm should not be completely disregarded, but 877 nm is generally considered to be the better option.

7.4 Conclusion

A computational model for simulating a laser generating near infrared nanosecond pulses has been implemented. The model includes both laser medium interactions, thermal effects in the laser rod and nonlinear effects. The model includes both the thermo-optical effect and end face expansion. The model has been compared to experimental results, showing a good correspondence in pulse energies given the uncertainty in simulation parameters. However, other features such as pulse width and radiant fluence does not seem to match the experimental results. The model was then used to optimize the design of a laser source with a set of given specifications. The final design produces 3.6 nanosecond long pulses with a tunable wavelength around $1.6\,\mu$m. The average pulse energy is 1.16 mJ with a beam quality $M^2 \simeq 2$.

7.5   Recommendations for further work

There are some issues that could be improved with further work. The first would be to implement the photoelastic effects. This effect was not implemented in Sisyfos at the time of writing, and could not be implemented. One possible solution is to find the equivalent phase shift due to the change in refractive index and implement this as an effective focal length.

The simulations were run without any thermal lensing and absorption in the KTA crystal. This was a result of time constraints. A thermal lens in the nonlinear crystal could be implemented in a similar manner as the thermal lens in the laser rod. The absorption could also reduce the efficiency of the conversion.

One possible way to reduce the thermal lensing in the laser rod is by using end caps. A laser rod with end caps has some undoped material attached to the end faces on the rod. The option for end caps was not implemented in the model due to time constraints.

While Nd:YLF was the most promising choice for the laser rod, Nd:YAG is also a viable candidate. A comparison between these two materials might be profitable, as YAG has some benefits over YLF (higher emission cross section, higher fracture limit). The change in thermal lensing might require a slightly different resonator as YAG has stronger positive lensing coming from a positive thermo-optical coefficient.

A final suggestion is a comparison between different nonlinear crystals. One possible choice could be KTP as it is similar to KTA. The transparency of the crystals and thermal effects should be implemented to make this comparison more realistic.

Appendix A

Derivations

A.1 Determining the phase matching angle

An analytical expression can be found for some specific types of phase matching in specific principal planes of the crystal. The following derivation finds the phase matching angle for type IIb phase matching (as defined in table 3.1) in the xz-plane of a uniaxial or biaxial material. The starting point is the phase matching criterion (3.16) and the index ellipsoid (figure 3.1)

$$\omega_3 n_o(\omega_3) = \omega_2 n_o(\omega_2) + \omega_1 n_e(\theta, \omega_1), \qquad \omega_3 = \omega_2 + \omega_1. \qquad \text{(A.1)}$$

In this expression, ω_3, ω_2 and ω_1 are the pump, signal and idler frequencies, with refractive index $n(\omega_i)$. The subscripts denote whether the corresponding wave is an o-wave or an e-wave. In this particular case, the values for the refractive index are so that the polarization in the xz-plane (e-wave) is slow, the o-waves in the xy-plane are fast. By substituting for the wavelength ($\omega = 2\pi c/\lambda$, c the speed of light), and inserting (3.1), the resulting expression becomes

$$\frac{n_{o3}}{\lambda_3} - \frac{n_{o2}}{\lambda_2} = \frac{1}{\lambda_1} \left(\frac{\cos^2 \theta}{n_{x1}^2} + \frac{\sin^2 \theta}{n_{z1}^2} \right)^{-1/2}, \qquad \text{(A.2)}$$

where for simplicity $n_o(\lambda_3)$ have been set to n_{o3} and so forth. Setting $n_{x1}/\lambda_1 = A$, $n_{o2}/\lambda_2 = B$, $n_{o3}/\lambda_3 = C$ and $n_{z1}/\lambda_1 = D$, and proceeding with squaring and inverting the expression gives

$$\frac{A^2}{(C-B)^2} = \frac{A^2}{D^2} \sin^2 \theta + \cos^2 \theta. \qquad \text{(A.3)}$$

This expression can be solved for θ, and yields

$$\tan^2\theta = \frac{1-T}{T-Z}; \quad T = \left(\frac{A}{C-B}\right)^2, \quad Z = \left(\frac{A}{D}\right)^2. \tag{A.4}$$

Similar expressions can be found for some other cases, tabulated in e.g. [27].

A.2 Derivation of the phase matching bandwidth

Conversion of a pump beam can occur for signal wavelengths that are not perfectly phase matched, as long as the phase mismatch is sufficiently small. This occurs in a given spectral bandwidth denoted the phase matching bandwidth.

To evaluate the phase matching bandwidth, the phase matching angle is assumed to be constant and the pump is assumed to have no bandwidth. The starting point is the phase matching intensity (3.15) in a crystal with lenght L. By constraining the changes in the intensity to no less than half the maximum value, the argument of the sinc-function is reduced to an interval

$$\left|\frac{\Delta k L}{2}\right| < 2.78. \tag{A.5}$$

Performing Taylor expansion to first order in the signal frequency

$$\Delta k(\omega_2 + \Delta\omega_2) = \frac{\partial \Delta k}{\partial \omega_2}\Delta\omega_2 \tag{A.6}$$

By demanding at least 50% efficiency (A.5), the total bandwidth becomes

$$|\Delta\omega_2| = \frac{5.56}{L|\mathrm{d}\Delta k/\mathrm{d}\omega_2|} \tag{A.7}$$

Evaluating the derivative in this expression at a constant pump frequency ω_3 and using that $\omega_1 = \omega_3 - \omega_2$ and $\omega = 2\pi c/\lambda$, the derivative becomes

$$\frac{\mathrm{d}\Delta k}{\mathrm{d}\omega_2} = \frac{1}{c}\left(-n_2 + \lambda_2\frac{\mathrm{d}n_2}{\mathrm{d}\lambda_2} + n_1 - \lambda_1\frac{\mathrm{d}n_1}{\mathrm{d}\lambda_1}\right) \tag{A.8}$$

Using $|\Delta\lambda| = \lambda^2|\Delta\omega|/2\pi c$, the expression for the phase matching bandwidth can be written in terms of wavelength as

$$L\Delta\lambda_2 = \frac{5.56\lambda_2^2}{2\pi\left[(n_1 - n_2) + \left(\frac{\mathrm{d}n_2}{\mathrm{d}\lambda_2} - \frac{\mathrm{d}n_1}{\mathrm{d}\lambda_1}\right)\right]} \tag{A.9}$$
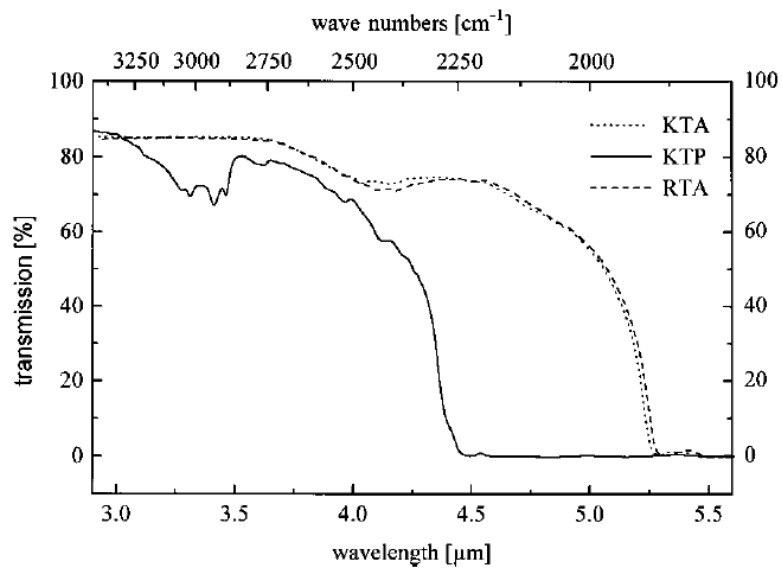
Appendix B

Supplementary figures

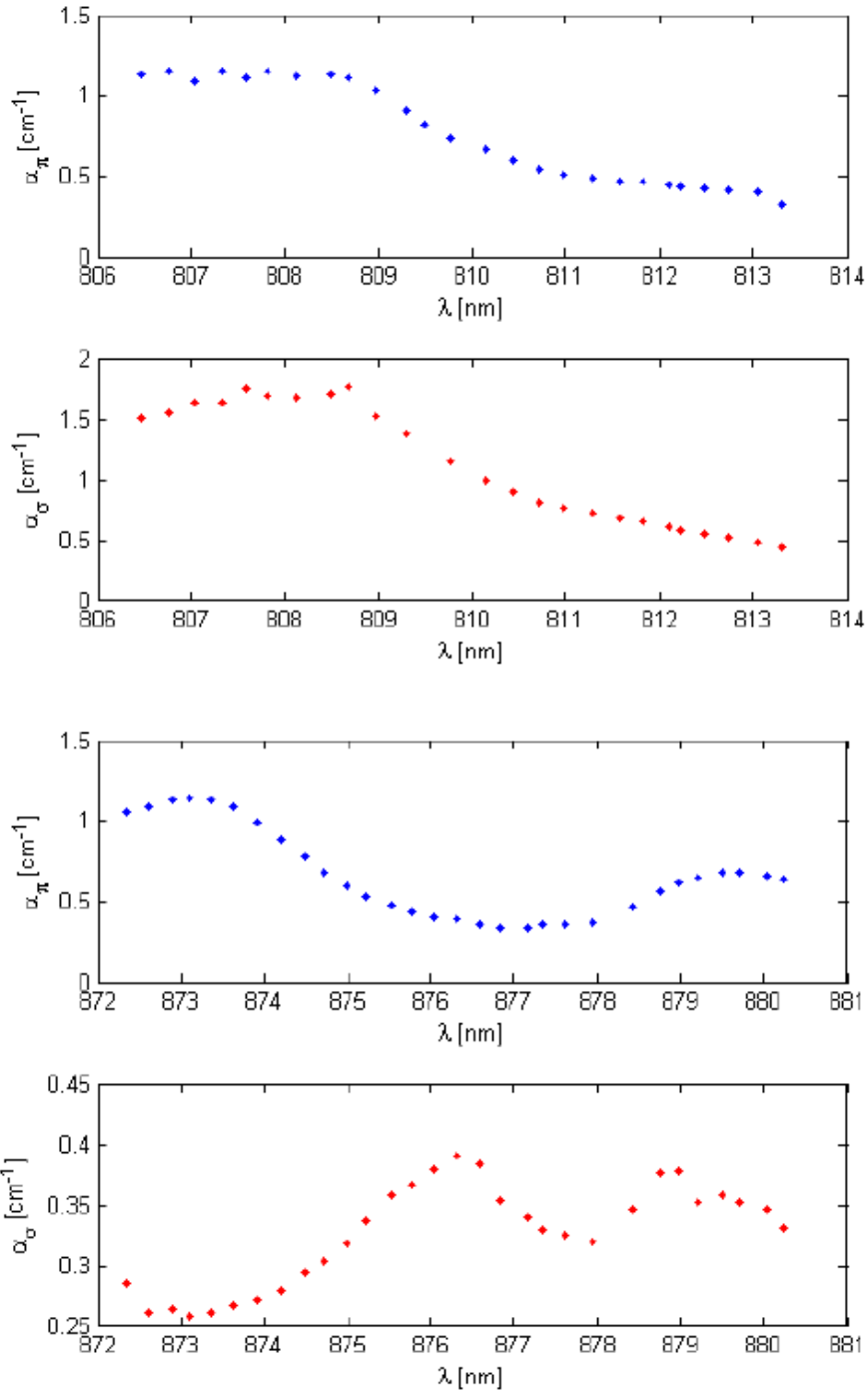Figure B.1: Transmittance of 3 mm thick KTP, RTA (RbTiOAsO$_4$) and KTA. Figure from Petrov et al. [38]

Figure B.2: Absorption in 0.9% doped Nd:YLF around 808 (top) and 877 nm (bottom) for π and σ-polarization. Figure from [35].

Bibliography

[1] Osama Bader and Harvey Lui. Laser Safety and the Eye: Hidden Hazards and Practical Pearls. "http://www.dermatology.org/laser/eyesafety.html", 1996. Online: Retrieved 26/11-2015.

[2] R. N. Clark. *Manual of Remote Sensing*, volume 3. John Wiley and Sons Inc., 1999.

[3] Rüdiger Paschotta. *Erbium-doped Fiber Amplifiers*. "https://www.rp-photonics.com/erbium_doped_fiber_amplifiers.html". Online: Retrieved 24/11-2015.

[4] Christophe Codemard, Carl Farrel, Pascal Dupriez, Valery Philippov, Jayanta K. Sahu, and Johan Nilsson. Millijoule, high-peak power, narrow-linewidth, sub-hundred nanosecond pulsed fibre Master-Oscillator Power-Amplifier at 1.55 μm. *Physique*, 7, 2006.

[5] Sebastien Desmoulins and Fabio Di Teodoro. High-gain Er-doped fiber amplifier generating eye-safe MW peak-power, mJ-energy pulses. *Optics Express*, 16, 2008.

[6] Rüdiger Paschotta. *Diode-pumped Lasers*. "https://www.rp-photonics.com/diode_pumped_lasers.html". Online: Retrieved 1/12-2015.

[7] Rüdiger Paschotta. *Optical Parametric Oscillators*. https://www.rp-photonics.com/optical_parametric_oscillators.html". Online: Retrieved 30/11-2015.

[8] M. Kenneth Oshman and Stephen E. Harris. Theory of Optical Parametric Oscillators Internal to the Laser Cavity. *IEEE Journal of Quantum Electronics*, 4, 1968.

[9] Ananada K. Cousins. Temperature and Thermal Stress Scaling In Finite-Length End-Pumped Laser Rods. *IEEE Journal of Quantum Electronics*, 28, 1992.

[10] C. Pfistner, R. Weber, H. P. Weber, S. Merazzi, and R. Gruber. Thermal Beam Distortions in End-Pumped Nd: YAG,Nd: GSGG, and Nd : YLF Rods. *IEEE Journal of Quantum Electronics*, 30, 1994.

[11] W. A. Clarkson. Thermal effects and their mitigation in end-pumped solid state lasers. *Journal of Physics D: Applied Physics*, 34, 2001.

[12] V. V. Zelenogorskii and E. A. Khazanov. Influence on the photoelastic effect on the thermal lens in a YLF crystal. *Quantum Electronics*, 40, 2010.

[13] Joel Falk, J. M. Yarborough, and E. O. Ammann. Internal Optical Parametric Oscillator. *IEEE Journal of Quantum Electronics*, 7, 1971.

[14] T. Debuisschert, J. Rafyy, J.-P. Pocholle, and M. Papuchon. Intracavity optical parametric oscillator: study of the dynamics in pulsed regime. *Journal of the Optical Society of America B*, 13, 1996.

[15] John E. Nettleton, Bradley W. Schilling, Dallas N. Barr, and Jonathan S. Lei. Monoblock laser for a low-cost, eyesafe, microlaser range finder. *Applied Optics*, 39, 2000.

[16] Rui Fen Wu, Kin Seng Lai, H. Wong, Wen-Jie Xie, Y. Lim, and Ernest Lau. Multiwatt mid-IR output from a Nd:YALO laser pumped intracavity KTA OPO. *Optics Express*, 8, 2001.

[17] Xiaoyuan Peng, Lei Xu, and Anand Asundi. Highly Efficient High-Repetition-Rate Tunable All-Solid-State Optical Parametric Oscillator. *IEEE Journal of Quantum Electronics*, 41, 2005.

[18] Fen Bai, Qingpu Wang, Zhaojun Liu, Xingyu Zhang, Xuebin Wang, Weixia Lan, Guofan Jin, Xutang Tao, and Youxuan Sun. Theoretical and experimental studies on output characteristics of an intracavity KTA OPO. *Optics Express*, 20, 2012.

[19] Orazio Svelto. *Principles of Lasers*. Springer, Fifth edition, 2010.

[20] Jens. O. Andersen. *Introduction to Statistical Mechanics*. Akademika Forlag, 2012.

[21] Frank L. Pedrotti, Leno M. Pedrotti, and Leno S. Pedrotti. *Introduction to Optics*. Pearson, 2014.

[22] George B. Arfken, Hans J. Weber, and Frank E. Harris. *Mathematical Methods for Physicists*. Academic Press, Seventh edition, 2013.

[23] Peter E. Powers. *Fundamentals of Nonlinear Optics*. CRC Press, 2011.

[24] Walter Koechner. *Solid State Laser Engineering*. Springer, Sixth edition, 2010.

[25] David J. Griffiths. *Introduction to Electrodynamics*. Pearson, Fourth edition, 2014.

[26] Gunnar Arisholm and Gunnar Rustad. *A review of theory and materials for optical parametric oscillators in the infrared*. FFI-report 1997/02589, 1997.

[27] Valentin G. Dmitrev, Gagik G. Gurzadyan, and David N. Nikogosyan. *Handbook of Nonlinear Optical Crystals*. Springer, Second edition, 1995.

[28] David N. Nikogosyan. *Nonlinear Optical Crystals, A Complete Survey*. Springer, 2005.

[29] Gunnar Arisholm and Helge Fonnum. *Simulation System For Optical Science (SISYFOS) - Tutorial*. FFI-rapport 2012/02042, 2012.

[30] J. Hellström, V. Pasiskevicius, H. Karlsson, and F. Laurell. High-power optical parametric oscillation in large-aperture periodically poled $KTiOPO_4$. *Optics Letters*, 25, 2000.

[31] David N. Nikogosyan. *Properties of Optical and Laser-Related Materials, A Handbook*. Wiley, 1998.

[32] Northrop Grumman. *Neodymium: Yttrium Lithium Fluoride - Nd:YLF*. "http://www.northropgrumman.com/BusinessVentures/SYNOPTICS/Products/LaserCrystals/Documents/pageDocs/Nd-YLF.pdf". Online: Retrieved 7/10-2015.

[33] W. R. Bosenberg, L. K. Cheng, and J. D. Bierlein. Optical parametric frequency conversion properties of $KTiOAsO_4$. *Applied Physics Letters*, 65, 1994.

[34] Govindhan Dhanaraj, Kullaiah Byrappa, Vishwanath Prasad, and Michael Dudley. *Springer Handbook of Crystal Growth*. Springer Science & Business Media, 2010.

[35] Silje S. Fuglerud. *Sommerprosjekt : Nd-laser*. Classification of diode pump lasers and absorption measurements, August 2014.

[36] R. L. Aggarwal, D. J. Rippin, J. R. Ochoa, and T. Y. Fan. Measurement of thermo-optic properties of $Y_3Al_5O_{12}$, $Lu_3Al_5O_{12}$, $YAIO_3$, $LiYF_4$, $LiLuF_4$, BaY_2F_8, $KGd(WO_4)_2$, and $KY(WO_4)_2$ laser crystals in the 80-300 K temperature range. *Journal of Applied Physics*, 98, 2005.

[37] Christoph Bollig, Cobus Jacobs, M. J. Daniel Esser, Edward H. Bernhardi, and Hubertus M. von Bergmann. Power and energy scaling of a diode-endpumped Nd:YLF laser through gain optimization. *Optics Express*, 18, 2010.

[38] Valentin Petrov, Frank Noack, and Richard Stolzenberger. Seeded femtosecond optical parametric amplification in the mid-infrared spectral region above 3 μm. *Applied Optics*, 36, 1997.